

Fall 2021

Dynamic Modeling of Soft Robotic Dielectric Elastomer Actuator

Abdullah De Jesus El Atrache Ceballos

Follow this and additional works at: <https://commons.erau.edu/edt>



Part of the [Mechanical Engineering Commons](#)

This Dissertation - Open Access is brought to you for free and open access by Scholarly Commons. It has been accepted for inclusion in PhD Dissertations and Master's Theses by an authorized administrator of Scholarly Commons. For more information, please contact commons@erau.edu.

**DYNAMIC MODELING OF SOFT ROBOTIC DIELECTRIC ELASTOMER
ACTUATORS**

By

Abdullah De Jesus El Atrache Ceballos

A Dissertation Submitted to the College of Engineering

Department of Mechanical Engineering in the College of Engineering

in Partial Fulfillment of the Requirements

for the Degree of

Doctoral of Philosophy

in

Mechanical Engineering

Embry-Riddle Aeronautical University

Daytona Beach, Florida

Fall 2021

DYNAMIC MODELING OF SOFT ROBOTIC DIELECTRIC ELASTOMER ACTUATORS

By

Abdullah De Jesus El Atrache Ceballos

This dissertation was prepared under the direction of the candidate's Committee Chairperson Dr. Eduardo Divo, Professor, Daytona Beach Campus, the Committee Co-Chair Dr. Daewon Kim, Associate Professor, Daytona Beach Campus, and has been approved by the Dissertation Committee. It was submitted to the Department of Mechanical Engineering in partial fulfillment of the requirements for the degree of Doctorate of Philosophy in Mechanical Engineering

Dissertation Review Committee:

Eduardo Divo

Eduardo Divo, Ph.D.
Committee Chair

Daewon Kim

Daewon Kim, Ph.D.
Committee Co-Chair

Eric J Coyle

Eric J Coyle, Ph.D.
Committee Member

Christopher Hockley

Christopher J Hockley, Ph.D.
Committee Member

Houbing Song

Houbing Song, Ph.D.
Committee Member

Eric J Coyle

Eric J Coyle, Ph.D.
Ph.D. Program Coordinator,
Mechanical Engineering

Eduardo Divo

Eduardo Divo, Ph.D.
Department Chair
Mechanical Engineering

Maj Dean Mirmirani

Maj Mirmirani, Ph.D.
Dean, College of Engineering

Lon Moeller

Lon Moeller, J.D.
Senior Vice President for Academic
Affairs and Provost

Date: 8/04/2021

Dedication

To God as thanks for all the miracles that he has done for me.

To my son Jesus, “What is and always will be my greatest creation, is you”

To my parents Rakan and Omaira for their unconditional love and for believing in me.

To my brother Rakan “More than a brother, an hermano”

To my system Maria Del Rosario, there is no love in this world like the one I have for
you.

To my wife Ansaf El Atrach, who supports me with strong love and perseverance
through these years while I was doing my Ph.D.

To my beautiful family.

Abstract

Dielectric elastomers actuators (DEAs) are among the preferred materials for developing lightweight, high compliance and energy efficient driven mechanisms for soft robots. Simple DEAs consist mostly of a homogeneous elastomeric materials that transduce electrical energy into mechanical deformation by means of electrostatic attraction forces from coated electrodes. Furthermore, stacking multiple single DEAs can escalate the total mechanical displacement performed by the actuator, such is the case of multilayer DEAs. The presented research proposes a model for the dynamical characterization of multilayer DEAs in the mechanical and electrical domain. The analytical model is derived by using free body diagrams and lumped parameters that recreate an analogous system representing the multiphysics dynamics within the DEA. Hyperelasticity in most elastomeric materials is characterized by a nonlinear spring capable of undergoing large deformation; thus, defining the isostatic nonlinear relationship between stress and stretch. The transient response is added by employing the generalize Kelvin-Maxwell elements model of viscoelasticity in parallel with the hyperplastic spring. The electrostatic pressure applied by the electrodes appears as an external mechanical pressure that compress the material; thus, representing the bridge between the electrical and mechanical domain. Moreover, DEAs can be represented as compliant capacitors that change their capacitance as it keeps deforming; consequently, this feature can be used for purposes of self-sensing since there is always a capacitance value that can be mapped into the actual displacement. Therefore, an analytical model of an equivalent circuit of the actuator is also derived to analyze the changes in the capacitance while the actuator is under duty.

The models presented analytically are then cross-validated by finite element methods using COMSOL Multiphysics[®] as the software tool. The results from both models, the analytical and FEM model, were compared by virtually recreating the dynamics of a multilayer DEA with general circular cross section and material parameters from VHB4905 3M commercially available tape. Furthermore, this research takes the general dynamical framework built for DEAs and expand it to model the dynamical system for helical dielectric elastomer actuators (HDEAs) which is a novel configuration of the classical stack that increases the nonlinearity of the system. Finally, this research present a complementary study on enhancing the dielectric permittivity for DEAs, which is an electrical material property that can be optimized to improve the relationship between voltage applied and deformation of the actuator.

Table of Contents

Dedication	I
Abstract	II
Table of Contents	IV
List of Figures	VII
List of Tables	XII
List of Symbols	XIII
List of Abbreviations	XVIII
Chapter 1 Introduction	1
1.1 Motivation.....	1
1.2 Research task	4
1.3 Dissertation Outline	5
Chapter 2 Literature Review	7
2.1 Soft Robots.....	7
2.2 Artificial Muscles.....	9
2.3 Electroactive Polymers	11

2.4	Applications	12
2.5	Modeling of dielectric elastomer actuator	16
2.6	Dielectric constant on dielectric elastomer actuators (DEA).....	19
2.7	Hyperelasticity theory	20
Chapter 3	Dynamical Modeling and FEM Validation of Soft Robotic Multi-layer Stacked Dielectric Elastomer Actuators	23
3.1	MULTILAYER DEA WORKING PRINCIPLE.....	23
3.2	FREE BODY DIAGRAM & DYNAMICS.....	25
3.3	SELF SENSING	33
3.4	THE ACTUATOR AND FEM.....	34
3.5	RESULTS	40
3.6	Control systems.....	46
3.7	CONCLUSIONS.....	48
Chapter 4	A dynamic model of helical dielectric elastomer actuator	50
4.1	Introduction.....	50
4.2	HDEA geometrical structure.....	50

4.3	Principal stretches of the HEDA.....	55
4.4	Free body diagrams and dynamics.....	58
4.5	Power consumption.....	66
4.6	RESULTS AND ANALYSIS.....	70
4.7	Actuator geometrical parameters	70
	Material parameters	71
4.8	Actuator dynamic responses	73
4.9	CONCLUSION AND FUTURE WORK	79
Chapter 5	Enhancing the Dielectric Constant of Dielectric Elastomer	
Actuators	81	
5.1	Introduction.....	81
5.2	Composite formulation	81
5.3	Experiment.....	83
5.4	Results.....	86
5.5	Conclusions.....	89

List of Figures

<i>Figure 1.1.</i> a) Soft robotic fish for underwater exploration (Katzschmann et al., 2018), b) Dielectric elastomer fish thins (Berlinger et al., 2018), c) Soft robotic gripper for food handling (Yamanaka et al., 2020), d) DEA biomimetic lenses (Gu et al., 2017a), and e) Soft robotic hand exoskeleton actuated with PAM (Al-Fahaam et al., 2018).....	4
<i>Figure 1.2.</i> Diagram shows the research workflow of this study.	6
<i>Figure 2.1.</i> Soft robotic fish (Rus & Tolley, 2015).	8
<i>Figure 2.2.</i> Cable-driven finger (Mohammadi et al., 2020).	10
<i>Figure 2.5.</i> DEA flapping wing robot (R. Pelrine et al., 2017).	12
<i>Figure 2.6.</i> DEA rotary joints assembled to form a flapping wing (J. Zhao et al., 2015).	13
<i>Figure 2.7.</i> Lower limb exoskeleton (Joudzadeh et al., 2019)	14
<i>Figure 2.3.</i> Working principle of dielectric elastomer actuators (DEAs).	18
<i>Figure 2.4.</i> Different geometrical configurations of DEA, (a) planar actuator, (b) circular stacked actuator, (c) folded actuator, (d) helical dielectric elastomer actuator HDEA.....	18
<i>Figure 3.1.</i> Single DEA “Sandwich” principle of work.	24
<i>Figure 3.2.</i> Multi-layer DEA structure	25

<i>Figure 3.3.</i> Actuator free body diagram and lumped parameter analogous mechanical system in the z-axis.	26
<i>Figure 3.4.</i> The amount of actuator mass being accelerated over time.	27
<i>Figure 3.5.</i> Free body diagram and lumped parameters in the radial axis.....	31
<i>Figure 3.6.</i> Open loop dynamics of multilayer DEA.....	33
<i>Figure 3.7.</i> (a) Single DEA “Compliant capacitor”, (b) Equivalent circuit lumped parameter model.	34
<i>Figure 3.8.</i> Mesh and multilayer DEA actuator (axisymmetric).	39
<i>Figure 3.9.</i> COMSOL Multiphysics model builder set up.	40
<i>Figure 3.10.</i> Comparison from analytical and numerical models.	41
<i>Figure 3.11.</i> Actuator displacement under 10 Hz cyclic voltage input demonstrating hysteresis.	43
<i>Figure 3.12.</i> Voltage input for Figure 3.10.....	43
<i>Figure 3.13.</i> Actuator displacement under 50 Hz cyclic voltage input demonstrating hysteresis.	44
<i>Figure 3.14.</i> Voltage input for Figure 3.12.....	44
<i>Figure 3.15.</i> Actuator displacement under 100 Hz cyclic voltage input demonstrating	

hysteresis.	45
<i>Figure 3.16.</i> Voltage input for Figure 3.10.....	45
<i>Figure 3.17.</i> PID tracking a triangle wave trajectory.	47
<i>Figure 3.18.</i> PID command output.	47
<i>Figure 3.19.</i> Actuator capacitance while tracking the triangle trajectory.....	48
<i>Figure 4.1.</i> (a) Shows the HDEA geometrical structure, (b) shows the relation of the thickness $z(t)$ of the elastomer and the electrode distance $h(t)$ by using the complementary angle $\alpha(t)$	52
<i>Figure 4.2.</i> Representation of the areas that encloses the volume of a HDEA.....	55
<i>Figure 4.3.</i> (a) Free body diagram of the forces in the z-axis, (b) Lumped parameter model in the z direction.	59
<i>Figure 4.4.</i> Lumped parameter model in the direction of the helical curve L_r	62
<i>Figure 4.5.</i> (a) 2D representation of the internal lumped parameter model of the mechanical reactions that causes the deformation of $\Delta R(t)$, (b) conservative simplification of the 2D model.....	65
<i>Figure 4.6.</i> (a) HDEA with voltage applied by connecting wires to the actuator, (b) Lumped parameter analogy of the electrical system of the HDEA.....	67
<i>Figure 4.7.</i> Open loop response of the HDEA.....	69

<i>Figure 4.8.</i> (a) Sub-System A of the open loop response in Figure 4.7, (b) Sub-System B of the open loop response in Figure 4.7, (c) Sub-System C of the open loop response in Figure 4.7.	70
<i>Figure 4.9.</i> Transient response of a step input voltage. On top actuator length vs. time, bottom voltage applied vs. time.	74
<i>Figure 4.10.</i> Transient response of a step input voltage.	75
<i>Figure 4.11.</i> Transient response of an input voltage with form of a sinusoidal wave.	75
<i>Figure 4.12.</i> Deformation of the actuator length under different loads without the presence of the electrostatic pressure.	76
<i>Figure 4.13.</i> Deformation of the actuator length and principal stretches while holding different loads under electrostatic pressure.	77
<i>Figure 4.14.</i> Complementary angle $\alpha(t)$ vs. time when the HDEA is under the conditions shown in <i>Figure 4.13</i>	78
<i>Figure 4.15.</i> Current and power consumption vs voltage and time when the HDEA is under the conditions shown in <i>Figure 4.13</i>	79
<i>Figure 5.1.</i> Generic polymer matrix mixed with fillers of high dielectric constant.	82
<i>Figure 5.2.</i> Coupon of plain BJB TC-5005.	84
<i>Figure 5.3.</i> THINKY MIXER ARE-310.	84

<i>Figure 5.4.</i> LCR meter and composite for capacitance measurement.	86
<i>Figure 5.5.</i> BJB TC-5005 (45% of C) combined with BaTiO ₃ add different volume fractions.	87
<i>Figure 5.6.</i> Measure of dielectric constant of Sylgard 184 composite that is mixed in a (15:1) ratio with the addition of BaTiO ₃ fillers at different weight fractions, and tested at different frequencies.	88
<i>Figure 5.7.</i> Measure of dielectric constant of Sylgard 184 composite that is mixed in a (15:1) ratio with the addition of CCTO fillers at different weight fractions, and tested at different frequencies.	89

List of Tables

Table 3.1. Initial condition for geometry of the cylindrical multilayer DEA	35
Table 3.2. Material parameters for VHB4910 for Yeoh model.	36
Table 3.3. Viscoelastic parameters of VHB4910 for Yeoh model.	37
Table 3.4. Complementary mechanical and electrical materials parameter of VHB4910 and actuator design.	38
Table 3.5. Percentage of RSME error between analytical and FEM models at step input voltages.	42
Table 3.6. Percentage of RSME error between analytical and FEM models from triangle wave input voltages	46
Table 4.1. Initial elementary parameters of the HDEA.	71
Table 4.2. Hyperelastic and viscoelastic material parameters.	73
Table 4.3. Electrical properties of the elastomer used.	79
Table 5.1. Elastomeric materials to be used as a polymer matrix.	83

List of Symbols

Chapter 1

$A_e(t)$	Surface area of the elastomer covered with electrodes
$A_g(t)$	Single layer elastomer cross section area
$A_{r_{lo}}(t)$	External area of the actuator
$A_{r_{li}}(t)$	Internal area of the actuator cavity
c	Slant of the helix
C_{10}, C_{01}	Mooney-Rivlin model parameter
C_{i0}	Yeoh model parameter
C_{HDEA}	Capacitance of helical actuator
$\frac{dV(t)}{dt}$	Derivate of voltage with respect time
E	Electric field
F_z	Total force in the z direction
$F_{H-elastic_z}$	Elastic force in the z direction
F_{el_z}	Electrostatic force in the z direction
F_{visc_z}	Viscous force from the Kelvin-Voight element in the z direction
F_{MV_z}	Total viscous force from Maxwell element in the z direction
$F_{MW_{z_j}}$	Force from the nth element in the Maxwell arms in the z direction
F_{load_z}	Total load attached to the actuator in the z direction
F_{lr}	Total Force in the helical direction

$F_{el_{lr}}$	Total electrostatic force in the helical direction
$F_{visc_{lr}}$	Viscous force from the Kelvin-Voight element in the helical direction
$F_{load_{lr}}$	Total load attached to the actuator in the helical direction
$F_{H-elastic_{lr}}$	Elastic force in the helical direction
$F_{MV_{lr}}$	Total viscous force from Maxwell element in the helical direction
$F_{MW_{lr_j}}$	Force from the nth element in the Maxwell arms in the helical direction
$F_{\Delta r}$	Total force in the radial direction
$F_{H-elastic_{\Delta r}}$	Elastic force in the radial direction
$F_{visc_{\Delta r}}$	Viscous force from the Kelvin-Voight element in the radial direction
$F_{MV_{\Delta r}}$	Total viscous force from Maxwell element in the radial direction
$F_{MW_{\Delta r_j}}$	Force from the nth element in the Maxwell arms in the radial direction
g	Gravity
$h(t)$	Elastomer thickness
$I_1, I_2, , I_3$	Principal Invariants
$I(t)$	Electric current
I	Identity tensor

k_j	Nth spring element in the Maxwell arms
L_r	Length of helical curve
\dot{L}_r	Velocity at which helical curve deform
\ddot{L}_r	Acceleration at which helical curve deform
L_{r_0}	Initial length of the helical curve through the outside radius
L_{r_i}	Initial length of the helical curve through the inside radius
m_{load}	Mass of attached load
m_{HDEA}	Mass of the helical actuator
M_T	Total mass being displace through the z axis
$M_{T_{lr}}$	Mass being displaced in the helical direction
n_j	Nth dashpot element in the Maxwell arms
N_e	Number of elastomers in series
N_p	Number of periods in the actuator
N_v	Viscosity of Kelvin-Voight element
N_{MW}	Number of Maxwell element
$P(t)$	Pitch of the helix structure
$Power_{el}$	Electric power
R_D	Actuator resistance
R_L	Wires connections resistances
$R_o(t)$	External radius
$R_i(t)$	Internal Radius

R_{o_0}	Initial external radius
R_{i_0}	Initial internal radius
$\Delta R(t)$	Distance between internal and external radius
S_z	Strain in the actuator longitudinal direction
S_r	Strain in the radial direction
S_ϑ	Strain of the helical arc length of the actuator
$V(t)$	Voltage
Vol_0	Initial volume of actuator
W	Strain energy function
$z(t)$	Thickness of the actuator
$Z_T(t)$	Total length of the actuator
\dot{z}	Velocity of the actuator in the z direction
\ddot{z}	Acceleration of the actuator in the z direction
z_0	Initial thickness of the actuator
ε_0	Vacuum permittivity
ε_r	Relative permittivity
$\alpha(t)$	Complementary angle
$\lambda_z, \lambda_{\Delta r}, \lambda_{lr}$	Principal stretches
ρ	Actuator density
σ_i	Cauchy stress
σ_{el}	Electrostatic pressure

μ_i, α_i

Ogden model parameters

List of Abbreviations

BaTiO ₃	Barium Titanite
CCTO	Calcium copper titanite
DEA	Dielectric elastomer actuator
EAP	Electroactive polymer
EHD	Electrohydrodynamic
HDEA	Helical dielectric elastomer actuator
PAM	Pneumatic automatic muscle
SMA	Shape-memory alloy

Chapter 1 Introduction

1.1 Motivation

Soft robots, a new paradigm in robotics, are able to interact with complex and natural environments that traditional robots with rigid bodies find troublesome to interact. These biologically inspired robots empower their systems by including soft, flexible, and smart materials into their morphology. Soft robots capabilities include underwater navigation (Berlinger et al., 2018; Katzschmann et al., 2018), human enhancing and rehabilitation (Al-Fahaam et al., 2018; Ang & Yeow, 2019), industrial food handling (Yamanaka et al., 2020) and others Figure 1.1.

Soft robots tend to be identified by the type of actuation system that provide locomotion power. Different actuator strategies have been proposed such as pneumatic actuators (PAM) (Al-Fahaam et al., 2018), shape memory alloys (SMA) (Llewellyn-Evans et al., 2020), and electroactive polymers (EAP) (Runsewe et al., 2019). From the EAP group, the dielectric elastomer actuators (DEASs), DEAs are soft elastomeric films coated with electrodes that change their shape when an electric field is applied. The elastomeric materials have a very low Young's modulus; thus electrostatic pressure coming from electrodes under attraction compress the elastomer. DEAs stand out because of their extraordinary ability to undergo large deformations while exerting high forces which resemble mammalian muscle extraordinary characteristics (Gu et al., 2017a; Youn et al., 2020a).

Meanwhile, the study of DEAs encompass many ongoing research challenges. The fabrication of most DEAs presented in the literature are mostly handcrafted for rapid prototyping and testing capabilities. This brings issues with data repeatability and actuation performance (Jung et al., 2017). The utilization of 3D printing techniques such as polymer electrohydrodynamic (EHD) 3D printing offers an elegant solution to improve the overall quality of DEA (Y. Wang et al., 2021). However, because the almost infinite number of materials and chemical combinations that can be proposed to create DEA the 3D printing scheme has to be tailored for the desired material. Dispensing time, cure time, nozzle aperture, and material compatibility between electrodes and the main dielectric film are some of the characteristics that need to be studied to optimize and accomplish the 3D printing process. On the other hand, modeling of DEA is an active area of research that aims to develop new models that properly describe the physics involved in the actuation process. Once the material is electrical activate, the interplay between electrical and mechanical properties will provide the desired deformation. However, this deformation depends on the mechanical properties of the materials. Dielectric elastomers tend to achieve large deformations so linear models of elasticity do not properly represent the input-output relationship; thus, models of hyperelasticity and strain energy functions need to be used instead. Meanwhile, DEA desired characteristic of softness also yields an undesirable effect on the actuators in form of viscous losses which causes the actuator to keep deforming even though a constant stimulus input is applied, which lead to undesired displacement of the end effector of the actuator resulting in controllability issues for simpler control systems schemes. Finally, a majority of the

research conducted on DEA is to enhance the material properties (Brochu & Pei, 2010). Although, DEAs theoretically possess many electromechanical advantages that could improve the future of soft robotic actuation, they are also known for their issue of needing high voltage levels in order to perform and small amount of deformation. Thus, there is currently research oriented to combine polymer matrices with ceramic filler to increase the dielectric permittivity of the material leading to an optimization process that tend to reduce the amount of voltage needed to obtain a desire deformation (Sikulski et al., 2021). This research focuses on providing a general framework that can be used to model the complex response of the dynamical system of multilayered DEAs. Having a proper dynamical model of DEAs could lead to manufacturers and scientist being able to speed the process of optimization of the capabilities of the actuators while at the same time being able to be used as a framework for testing of new control systems that can be better adapted for the nonlinearities within DEAs intrinsic physics. Finally, this study also provides preliminary guidance on how to optimize the dielectric permittivity of elastomers by creating polymer composites by combining elastomeric materials with ceramic fillers. The study serves as a guideline on how to create polymer composites and to test the resulting electrical property as well to prove that mixing filler with polymer matrices leads to an increase of the parameter.

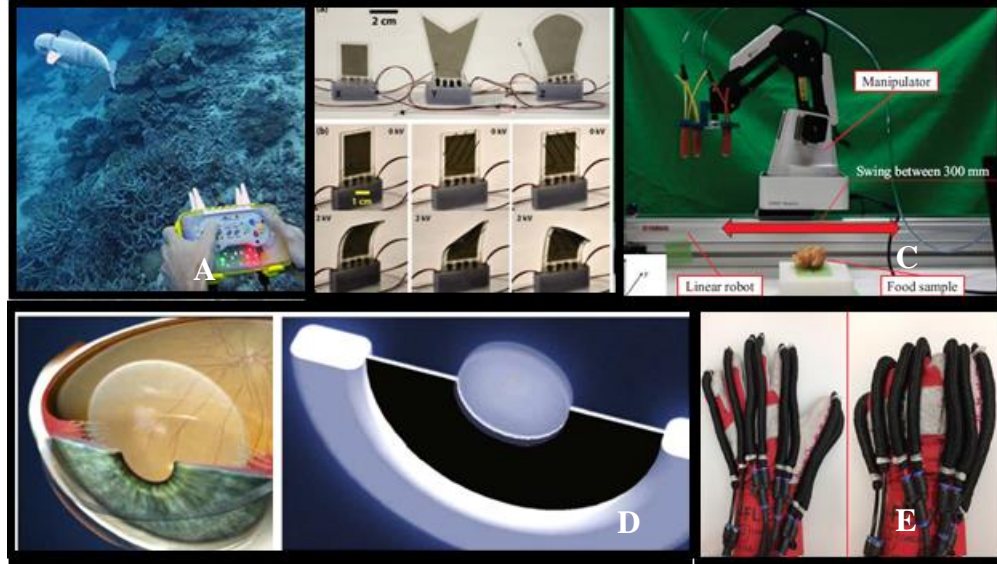


Figure 1.1. a) Soft robotic fish for underwater exploration (Katzschmann et al., 2018), b) Dielectric elastomer fish thins (Berlinger et al., 2018), c) Soft robotic gripper for food handling (Yamanaka et al., 2020), d) DEA biomimetic lenses (Gu et al., 2017a), and e) Soft robotic hand exoskeleton actuated with PAM (Al-Fahaam et al., 2018)

1.2 Research task

The objectives of this research are described as follows:

- a) To propose an analytical framework to model dynamics of multilayer dielectric elastomer actuators. Validation of the analytical model through finite element model FEM.
- b) Demonstration of generalization of the analytical model by employing the framework on the special case of the helical dielectric elastomer actuator (HDEA).

c) Demonstrate an improvement of the dielectric constant when ceramic fillers are mixed with a polymer matrix.

1.3 Dissertation Outline

The diagram presented on Figure 1.2 represents the workflow of this study and the chapters are organized.

Chapter 1 explains the motivation of this research as well as how the research is structured.

Chapter 2 presents a background of soft robotics as well as what are electroactive polymers and their different types. Finally, it goes over the principle of working on dielectric elastomer and the importance of the dielectric constant as a parameter to be optimized.

Chapter 3 introduces the framework for deriving dynamics of DEA and its validation through FEM.

Chapter 4 develops the dynamic equations for a special case of DEA, the helical configuration.

Chapter 5 is an experimental section that shows the procedures to create polymer composites with enhance dielectric permittivity.

Finally, the conclusion section at the end of this dissertation summarizes the important outcomes of this research and proposes future studies in the field.

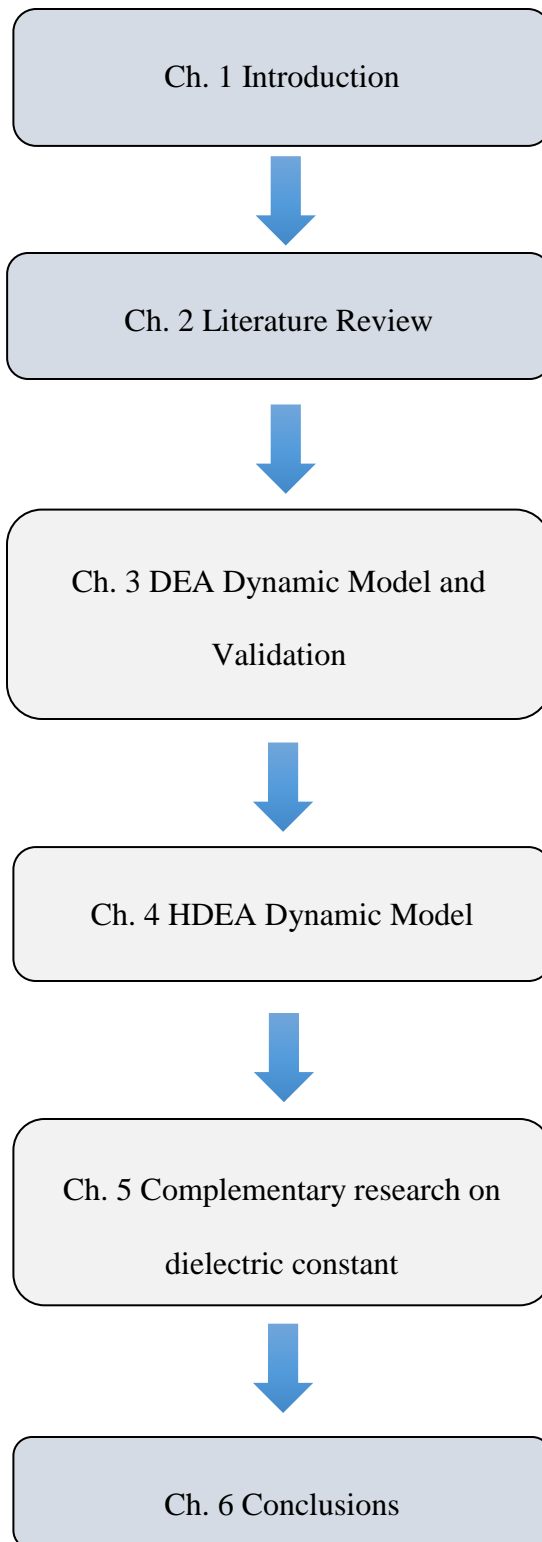


Figure 1.2. Diagram shows the research workflow of this study.

Chapter 2 Literature Review

2.1 Soft Robots

Through millions of years of evolution, animals have adapted body structures to optimize how they interact and maneuver through complex environments. The scientific community has drawn inspiration from these natural adaptations and are pursuing bio-inspired robotic designs such as a soft robotic fish (Figure 2.1). Leveraging soft robotics, traditional rigid robot designs can see benefits including increased system efficiency coupled with decreased system complexity in both mechanical and control system design (S. Kim et al., 2013). Soft robotics comprises most of these bio-mimicry devices. A novel category of these designs use smart materials that have multiple capabilities to execute actuation, measure their environment, and control (W. Cao et al., 1999) These soft robots embed these body control elements into a single structural morphology (Laschi & Cianchetti, 2014) which makes them reliable for diverse applications including robotic arms for space applications (Branz & Francesconi, 2017), grippers (W. Wang et al., 2016), and artificial muscles (J. Kim et al., 2017; Must et al., 2015).

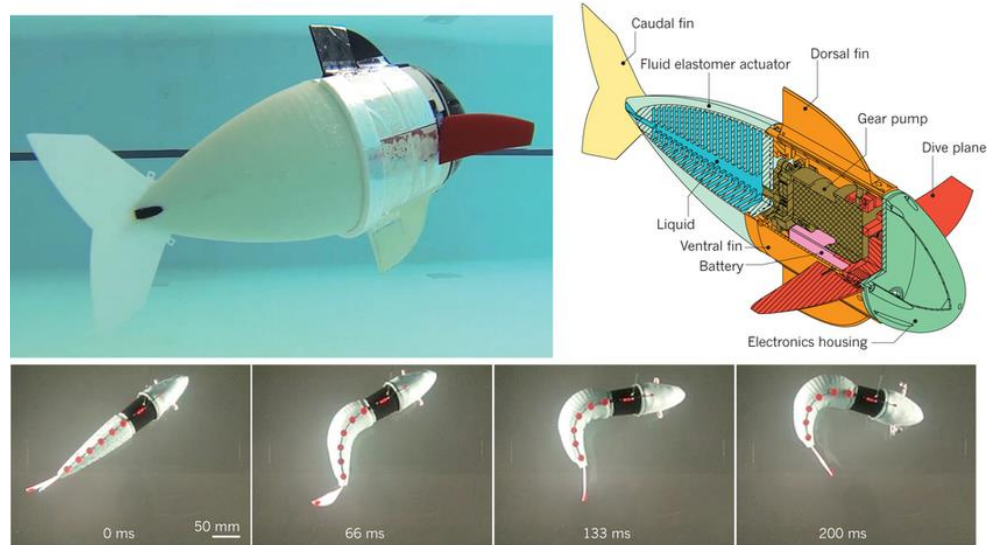


Figure 2.1. Soft robotic fish (Rus & Tolley, 2015).

Soft robots are characterized to have high degrees of freedoms because of their compliant and flexible morphology that allows them compress, extend, bend and twist in multiple directions, whereas traditional rigid actuators and robotic mechanisms are characterized by limited degrees of freedom because of the rigid links and actuators. As the nomenclature insinuates, soft robots are comprised of materials that can undergo large deformations elastically. This trait can be distinguished using the Young's modulus of the materials involved. For typical "rigid" robotic mechanisms, exhibit moduli over 10^9 Pa, while "soft" robotic mechanisms fall under 10^9 Pa (Rus & Tolley, 2015).

Overall, soft robotics can be broken down into three main categories in design considerations: actuation, sensing, and structure. Actuation approaches subsequently break down to length variable tendons such as tension cables and SMAs, fluidic actuators such as compliant pneumatic and hydraulic devices, and EAPs such as electronic and

ionic actuators. Soft sensors with moduli under 1 MPa provide an alternative means of proprioception feedback in applications with high deformation (Lee et al., 2017).

Structurally, materials such as rubbers, provide soft robots with compliant bodies that increases degrees of freedom while simultaneously maintaining stiffness, further expanding options for robot designs. Given the flexibility and the possibility to consolidate multiple design considerations, soft robotics provide an adaptable design medium that has the potential to simplify system complexity and offer more design opportunities to researchers and application developers.

2.2 Artificial Muscles

Early in the development of “artificial muscles,” length variable tendons and fluidic actuators dominated the field of these compliant mechanisms with deep historical roots in aviation and automotive applications. The 1903 Wright Flyer exemplifies an early use of length variable tendons (Advani et al., 2003). Fluidic actuators predate smart material use in actuators, as highlighted by patents such as the “pneumatic suspension system” (Kolstad & Tagg, 1984). These types of artificial muscles present unique design challenges. With tension cables and fluidic actuators, additional systems are necessary to drive these components and may exceed tight space constraints, such as a simulated human finger joints Figure 2.2; these driving systems, such as motors and pumps, would potentially need to be separated from the actuation site, giving rise to additional modes of failure and increased system complexity. In addition, these older artificial muscle designs may prove more imprecise in practice with stacked tolerances and the need for external

sensing.



Figure 2.2. Cable-driven finger (Mohammadi et al., 2020).

Many of the drawbacks faced by soft robotic artificial muscles have been overcome through the implementation of smart materials. An extensive range of these intelligent materials such as liquid crystal elastomers (Petsch et al., 2015), nanoporous metal-polymers (Detsi et al., 2015), carbon-nanotubes (Di et al., 2016), and others have been tested to search for the best choice for this application. However, electroactive polymers (EAPs) are gaining prominence as a preferred material in the field since they can mimic properties of true skeletal muscle actuation (Brochu & Pei, 2010; Mirfakhrai et al., 2007).

2.3 Electroactive Polymers

Electroactive polymers are smart materials that have the intrinsic characteristic of deforming when they are subjected to electrical stimulation. Depending on their material property response, they are classified into two major groups Electronic EAP and Ionic EAP. In the first group, electronic EAPs generate electrostatics forces that create dipoles that cause internal stresses called Maxwell Stresses that change the shape of the material by compressing it (Figure 2.6). On the second group, ionic EAPs are materials that respond when movement of the ions inside the material occurs when a voltage is applied (Mirfakhrai et al., 2007; Shankar et al., 2007).

One subclass of electronic EAPs (Dynamics & Forum, 2001; T. Wang et al., 2016), the dielectric elastomer actuator (DEAP), has advantages when mimicking muscle tissue. Large actuation forces and fast responses are some of the attractive characteristics that make DEAPs superior among different types. Depending on the material composition of the elastomer, some dielectric elastomers can reach strains up to 380% at high electric fields, which is higher than the typical 20% strain on the skeletal muscles of mammals (Mirfakhrai et al., 2007). An essential characteristic is that most elastomer actuators present typical thickness around the 100 μm ; therefore, to reach large strokes these actuators have to be combined in different forms (Carpi, Salaris, & de Rossi, 2007) in order to achieve more displacement, such as the stacked configuration and the helical configuration (HDEA) (Figure 2.7d).

2.4 Applications

DEA applications range from biomimicry to industrial. Insectoid robots such as the flapping wing robot in Figure 2.3 benefits from the simplicity of the form factor and the space-saving nature of the DEA design, combining desirable solid mechanics characteristics with power density (R. Pelrine et al., 2017). The technology offers the ability to create textures and localized morphologies that proves useful in optics and telecommunications applications such as switching, beamforming, active light directing (i.e., lidar, etc.), and active diffracting gratings (O'Halloran et al., 2008; Shian et al., 2013).

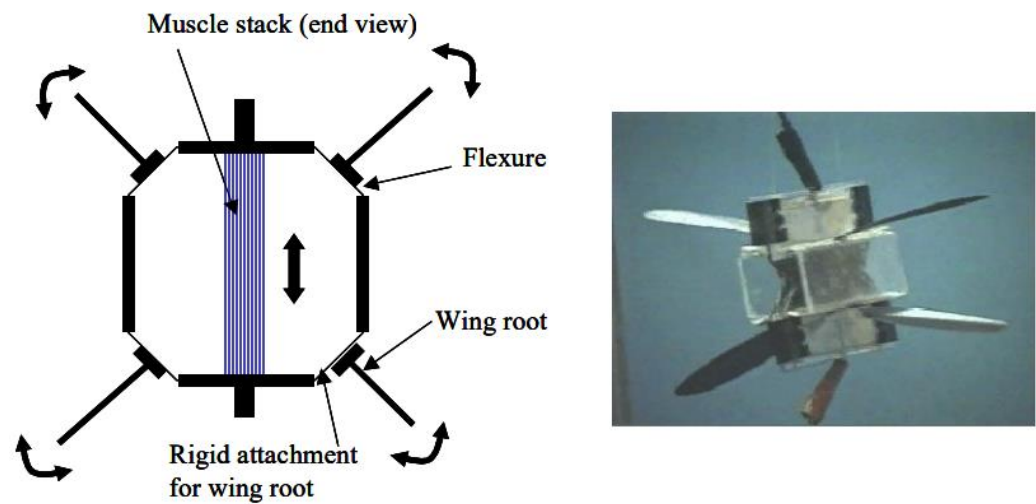


Figure 2.3. DEA flapping wing robot (R. Pelrine et al., 2017).

This capability for creating dynamic textures and unique morphologies extend to aerodynamics applications as well. Air flow can be modulated through manipulation of surface roughness (O'Halloran et al., 2008). Morphing wings and control surfaces such as

flaps can benefit from DEAs as seen in Figure 2.4 (C. Cao et al., 2019; J. Zhao et al., 2015).



Figure 2.4. DEA rotary joints assembled to form a flapping wing (J. Zhao et al., 2015).

The surface manipulation characteristics of DEAs further apply to diaphragm actuators such as loudspeakers and artificial hearts (O'Halloran et al., 2008; R. Pelrine et al., 2017), leading into a compelling use case for this genre of actuator: human aid and healthcare. Using these novel materials, powered prosthetics, artificial limbs, and powered exoskeletons can be realized. From helping workers stock warehouse shelves to rehabilitation, DEA use in developing human biomimetics shows promise.

An exoskeleton, in biology, is an external frame that supports inner organs in living organisms. The main purpose of an exoskeleton, from a technological perspective, is to protect and support the body where it is attached with and enhance human ability Figure 2.5.



Figure 2.5. Lower limb exoskeleton (Joudzadeh et al., 2019)

Majority of the work done in the early stages of studies on exoskeleton was mostly conceptual; nothing was essentially built or tested until the 1960s. Analysis by Ali (2014) stated that in the late 1960's, General Electric Research (Schenectady, NY), with Cornell University, created a full-body driven exoskeleton model. The exoskeleton was a massive hydraulically power-driven machine (680 kg) that contributed to augment the strength of the arms and limbs of the user. In the 1970s, Miodor Vukobratovic with his colleagues started to develop an exoskeleton known as "Kinematic Walker". This robot consists of a single hydraulic actuator for driving hip and the knee. Further work was done on it to make it a better driven machine. Their efforts resulted in a "partial active exoskeleton" which be made up of air-filled actuators for the hip, knee and ankle flexion (Ali, 2014). Generally, one of the applications in where exoskeletons are used is by people who suffer

from physical injuries, one of the most common causes being a stroke. According to Kotov et al. (2016) a study was conducted at the Department of Neurology, Vladimirskii Moscow Regional Research Clinical Institute in 2013–2014 on a small scale. It included a sum of five patients; four suffered from ischemic strokes, and one had a hemorrhagic stroke. These patients were treated with rehabilitation exercises. This is where the patient wears the electrode bearing cap for EEG data, and an exoskeleton is attached to the paralyzed part of the body, in this case, it was attached to the paralyzed hand. The result showed a positive change in neurological status. Meaning an increase in the range and movements of the paralytic hand, as well as improvements in sensory functions. (Kotov et al., 2016).

2.5 Modeling of dielectric elastomer actuator

Among smart material actuation methods, the use of dielectric elastomers stands out for promising due to their high energy density and strong similarities to natural muscle behavior (Duduta et al., 2019). DEAs can undergo large deformation when under an electric field and rapidly recover their original shape once the stimulus ceases (He et al., 2009; X. Zhao & Suo, 2010). Furthermore, DEAs exist in a diverse gamma of geometrical configurations (Alibakhshi & Heidari, 2020; Gu et al., 2017b; Youn et al., 2020b), to intentionally recreate a desire pattern of motion(D. Kim, Park, et al., 2019), to increase the amount of degrees of freedom (Conn & Rossiter, 2012; Nguyen et al., 2017), or to optimize the amount of deformation and power consumption of the actuator (C. Cao et al., 2020; D. Kim et al., 2018). Notoriously, one of the most useful representations is the longitudinal and single degree of freedom multilayer stack DEA (Carpi et al., 2005; Carpi, Salaris, & De Rossi, 2007; Kovacs et al., 2009) which consist of stacking multiple simple DEAs mechanically in series (Figure 2.7b). This research derives comprehensive analytical dynamics and purpose a finite element model for cross-modeling validation of a single degree of freedom multi-layer DEA configuration. First step while modeling DEAs is to combine the governing equations from the mechanical and electrical domain (Wissler & Mazza, 2007a). Stress-Strain relationships define the amount of deformation that the actuator can undergo when subjected to mechanical pressure. An electric field created when a voltage is applied can cause electrostatic attraction between the electrodes

within the actuator thus generating an electrostatic pressure that compresses each elastomeric layer. The electrostatic pressure can be characterized by using Maxwell's electrostatic pressure equation (Kofod et al., 2003; R. E. Pelrine et al., 1998a; Sahu et al., 2016) and when coupled with the stress-strain relationship from the mechanical domain, it concludes providing a model that governs the isostatic interplay between the actuator mechanical deformation and voltage electrical domain. Furthermore, one remarkable feature of DEAs is to have the ability of undergoing very large deformation and recovering its initial length. However, assuming the proportionality between stress and strain by using the Young's modulus cannot account for the nonlinear characterization of the material through large deformations. Therefore, the formulation has to be extended by using strain energy functions when the material presents a hyperelastic mechanical deformation (Wissler et al., 2005) which is the case of most elastomeric like materials (Ali et al., 2010; Khajehsaeid et al., 2013). Moreover, the chemical structure of the elastomers are commonly exploited with the intention to increase the softness in the material to decrease the amount of voltage needed for actuation (Hu et al., 2020); however, an increase in softness can sometimes rebound in the viscous responses that prolongs the deformation of the film over time preventing precise and stable actuation control (Tan et al., 2019). Thus, it is imperative to couple the isostatic electromechanical modeling with viscoelasticity governing equations to understand the transient mechanics of the system (J. Zhang, Chen, et al., 2017). In this research we utilize the generalized Kelvin-Maxwell lumped parameter model (Fancello et al., 2006a) to characterize the nonlinear viscous response of the elastomer over time. Finally, after characterizing all the

necessary multiphysics involved in the internal material dynamics, representing the actuator with a free body diagram and analogous lumped parameter modeling come convenient to organize all the external and internal forcers and their line of action for their projections depending on the actuator geometry and principal directions of study (Hoffstadt & Maas, 2015a; D. Kim, El Atrache, et al., 2019).

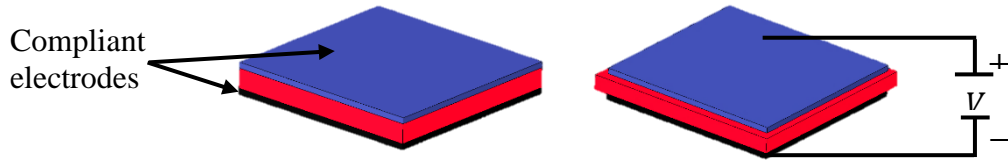


Figure 2.6. Working principle of dielectric elastomer actuators (DEAs).

$$\sigma_{el} = \varepsilon_0 \varepsilon_r E^2 = \varepsilon_0 \varepsilon_r \left(\frac{V}{h} \right)^2 \quad (2.1)$$

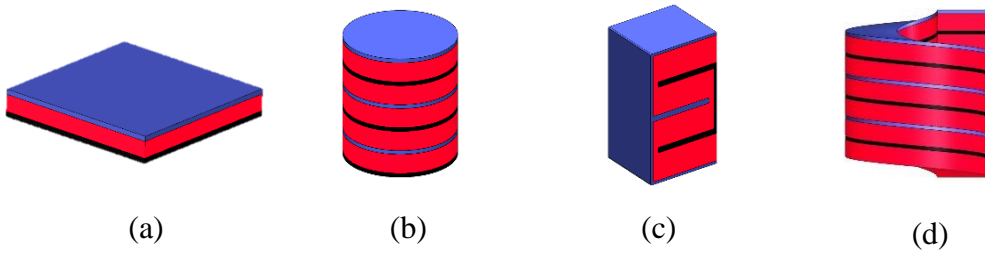


Figure 2.7. Different geometrical configurations of DEA, (a) planar actuator, (b) circular stacked actuator, (c) folded actuator, (d) helical dielectric elastomer actuator HDEA.

2.6 Dielectric constant on dielectric elastomer actuators (DEA)

The dielectric constant or relative permittivity is a parameter that aims to describe the performance of dielectric elastomer actuators (DEAs) and it is been quantified to be linear related to the merit of the material in study. The merit of the material is a unitless parameter that is proportional to the dielectric constant and inversely proportional to the Young's modulus of the material in study, the idea is to try to increase the ratio between dielectric constant and Young's modulus. Thus, an ideal material will have a very high dielectric constant while simultaneously being very soft (Sommer-Larsen & Larsen, 2004). An increase on the dielectric constant of the material means that the voltage required to create the electrostatic pressure that compress the elastomer can be reduced which is an imperative fact since most known DEAs use high voltage to function.

However, It is been proven that different factors can affect the intensity of the dielectric constant, studies on acrylics and silicone elastomers have shown that as the material get stretched the dielectric constant tends to decrease (Kurimoto et al., 2018; Schlögl & Leyendecker, 2017). Furthermore, depending on the nature of the elastomer such as acrylics, the dielectric constant can decrease at higher operation frequencies (Bindu.SI*, H.A Mangalvedekar¹ & Archana Sharma², D. P. Chakravarti², P.C Saro/, 2012; Jean-Mistral et al., 2010a), instead on PDMS the dielectric constant can remain unchanged as frequency increases. Meanwhile, when PDMS are used for creating composites, the obtained dielectric constant from the mixture tends to depend of frequency rates (Madsen et al., 2014). As a consequence of a lack of commercial silicones with a high dielectric constant, different techniques to enhance the dielectric constant of the material have been

purposed on the literature. Polymer blends and chemically modified silicones are some of the effective options on enhancing the dielectric properties of the materials, however, one of the method most commonly used is the creation of silicone composites by the introduction of fillers (Madsen et al., 2016a). The creation of silicone composites offer a fast and simple approach to increase the dielectric permittivity of the material, a wide range of metal oxides such as BaTiO₃ and CCTO are some of the most common used because of their high dielectric constant, however, attention has to be taken since an increase on the weight fraction of the filler in the elastomer can bring an increase of the Young's modulus (Madsen et al., 2016a; Romasanta & Verdejo, 2015), thus, the overall merit of the material may not increase significantly. Another, approach is the use of conductive fillers such as MWCNT into the polymer matrix, however, this may also increase the conductivity of the material which is an undesired objective in this case (Shehzad et al., 2015). Finally, depending of the particle shapes and size added to the mixture, silicone composites can be rapidly be created an used in additive manufacturing techniques such as micro dispensing for rapid prototyping (Robles et al., 2018).

2.7 Hyperelasticity theory

Hyperelastic materials offer a versatile solution for applications that require products that non-permanently deform when subjected to large strains. Resolving the non-linear behavior of these elastomer materials require sophisticated models to characterize strain energy. The Mooney-Rivlin, Yeoh, and Ogden models for strain energy exemplify models used to predict hyperelastic material behavior.

The strain energy ' W ' is a function of the invariants I_1, I_2, I_3 determined by eigenvalues of the Cauchy-Green deformation gradient tensor (Shahzad et al., 2015).

$$W = f(I_1, I_2, I_3) \quad (2.2)$$

Where the first invariant and second invariant can be calculated from the principal stretch ratios (Shahzad et al., 2015; Wissler & Mazza, 2005b) $\lambda_1, \lambda_2, \lambda_3$:

$$I_1 = \lambda_1^2 + \lambda_2^2 + \lambda_3^2 \quad (2.3)$$

The Second Invariant:

$$I_2 = \lambda_1^{-2} + \lambda_2^{-2} + \lambda_3^{-2} \quad (2.4)$$

The Third Invariant (assuming the material is incompressible) becomes:

$$I_3 = \lambda_1^2 \lambda_2^2 \lambda_3^2 = 1 \quad (2.5)$$

Therefore, the strain energy function can be redefined in terms of I_1 and I_2

$$W = W(I_1 - 3, I_2 - 3) \quad (2.6)$$

These strain energy models each offer different strengths and weaknesses (García Ruíz & Yarime Suárez, 2006). The Yeoh and Ogden models accurately describe the stress-strain

relationship of hyperelastic material at large deformation, while the Mooney-Rivlin Model can fail to represent the response of the material depending on the number of parameters selected for the model. The Yeoh Model predicts behavior with minimal data unlike the Ogden Model. Material parameters for these models such as $C_{10}, C_{01}, C_{i0}, \mu_i, \alpha_i$ are determined by subjecting the material to uniaxial, biaxial, planar, and volumetric tests. The appropriate model can be selected by comparing the best fit of the model predictions to experimental observations and material parameters can be extracted from curve fitting.

The Mooney-Rivlin Two Parameters Model:

$$W = C_{10}(\bar{I}_1 - 3) + C_{01}(\bar{I}_2 - 3) \quad (2.7)$$

The Yeoh Model:

$$W = \sum_{i=1}^3 C_{i0}(\bar{I}_1 - 3)^i \quad (2.8)$$

The Ogden Model:

$$W = \sum_{i=1}^N \frac{2\mu_i}{\alpha_i^2} (\bar{\lambda}_1^{\alpha_i} + \bar{\lambda}_2^{\alpha_i} + \bar{\lambda}_3^{\alpha_i} - 3) \quad (2.9)$$

Furthermore, for a material that is considered to be incompressible, a hydrostatic pressure

P term (Goriely et al., 2006) is accounted for to calculate the Cauchy stress σ_i :

$$\sigma_i = \lambda_i \frac{\partial W}{\partial \lambda_i} - P \quad (2.10)$$

Chapter 3 Dynamical Modeling and FEM Validation of Soft Robotic Multi-layer Stacked Dielectric Elastomer Actuators

3.1 MULTILAYER DEA WORKING PRINCIPLE

A single “sandwich” DEA consist of a soft elastomeric film coated with conductive electrodes which are preferably compliant as well. The application of voltage between electrodes generate electrostatic attraction forces from opposite charges that compress the elastomeric film, thus; transducing electrical energy into mechanical motion by means of induced deformation (*Figure 3.1*). The total electrostatic pressure exerted over the elastomeric film can be computed with Maxwell electrostatic equation (3.1) (R. E. Pelrine et al., 1998b). Notice, the electrostatic pressure is proportional to the square of the electric field E applied and the permittivity ϵ of the elastomer. The absolute permittivity ϵ depends on the vacuum permittivity $\epsilon_0 = 8.85 * 10^{-12} \text{ F/m}^{-1}$ and the dielectric permittivity ϵ_r from the elastomer material constitution (Caspari et al., 2018; Madsen et al., 2014; Yu et al., 2015). Having a higher dielectric permittivity ϵ_r indicates that the dielectric material possess a higher capacity to stored electrostatic energy. Therefore, ϵ_r is considered a merit parameter that when optimized leads to achieve higher amount of

electrostatic pressure while decreasing the required driving voltage of actuation (Della Schiava et al., 2018). Meanwhile, the maximum amount of voltage a DEA can withstand is determined by its dielectric strength which warns that an increase on the electric field as the thickness of the dielectric z_d gets thinner could lead to dielectric breakdown (Zurlo et al., 2017).

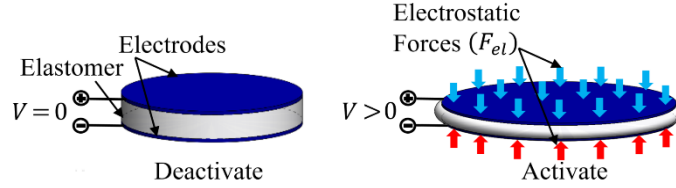


Figure 3.1. Single DEA “Sandwich” principle of work.

$$\sigma_{el_z} = \varepsilon E^2 = \varepsilon_r \varepsilon_o \left(\frac{V}{z_d} \right)^2 \quad (3.1)$$

A multi-layer DEAs consist on mechanical stacking multiple “sandwich” of single DEAs in series and electrical in parallel (Figure 3.2). The stack configurations are built within many actuator layers and the compression force is equally conserved along each layer on the actuation direction (Kovacs et al., 2009). The total length of the actuator Z_T depends of the number of layers of dielectric films n_d and electrodes n_e as well as their thickness n_d and n_e respectively (3.2).

$$Z_T(t) = n_d z_d(t) + n_e z_e(t) \quad (3.2)$$

The presented dynamic modeling is centered on the dielectric material, and the following

assumptions are made. The electrodes are very small in thickness compared with the dielectric film; thus, change in thickness of electrodes is almost negligible. Electrodes are made from an ideal compliant material with high conductivity, which can deform equally as the elastomeric film without preventing mechanical expansion in the radial direction. Therefore, we assumed that the change in the principal stretches on the elastomeric film λ_{d_z} and λ_{d_r} are equal to the changes in the electrode principal stretches λ_{e_z} and λ_{e_r} over time. Equation (3.2) can be rewritten as a function of the principal stretch of the elastomers in the z direction $\lambda_{d_z}(t)$ (3.3).

$$Z_T(t) = n_d \lambda_{d_z}(t) z_{d_0} + n_e \lambda_{d_z}(t) z_{e_0} \quad (3.3)$$

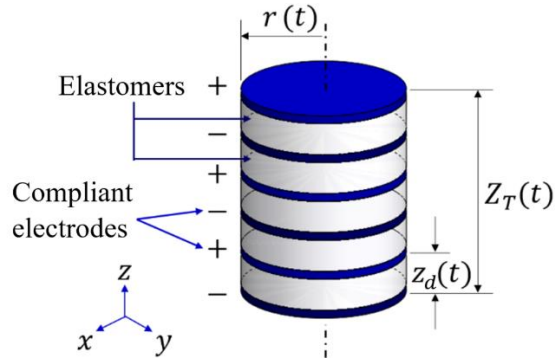


Figure 3.2. Multi-layer DEA structure

3.2 FREE BODY DIAGRAM & DYNAMICS

Multilayer DEA dynamic equations can be derived from analyzing the external forces that act over the actuator such as electrostatic forces F_{el} (3.7) that attempt to compress the material or attached loads F_{load_z} (3.9) that can pull against or resist to the actuator free

motion. These external forces create reactions inside the material that governs the internal structural dynamics. Accordingly, Elastic reaction forces such as F_{elast} (3.11) leads to static deformation of the elastomer, and viscous forces F_{vis} , F_{MW} will drive the transient deformation (3.13)(3.14). Sketching a free body diagram of the actuator and creating an analogous lumped parameter of the electromechanical system as shown in (Figure 3.3) assist to formulate a summation of forces and extract the differential equations that governs the actuator motion.

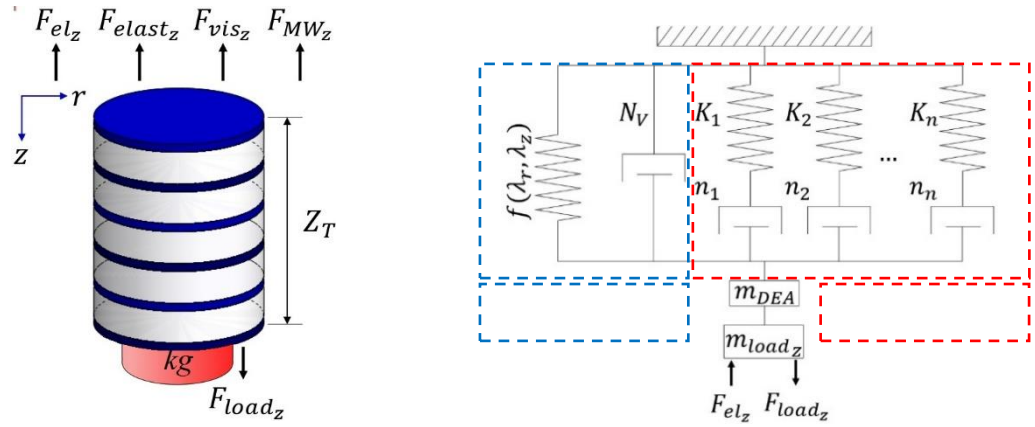


Figure 3.3. Actuator free body diagram and lumped parameter analogous mechanical system in the z-axis.

The free body diagram in (Figure 3.3) comprise all the acting forces in longitudinal axis of the actuator (z-axis) and the summation of forces leads to differential Equation (3.4).

The summation of force is equivalent to the total force acting on z-axis F_z , where M_{acc} is the

$$\sum F_z: F_{load_z} - F_{el_z} - F_{elast_z} - F_{vis_z} - F_{MW_z} = M_{acc}\Delta\ddot{z} = F_z \quad (3.4)$$

M_{acc} is a summation from any mass m_{load_z} attached to the actuator, and the total volume of actuator mass m_{DEA_z} that is being displaced while the actuator is deforming $M_{acc} = m_{load_z} + m_{DEA_z}$. The displaced mass m_{DEA_z} is derived in Equation (3.5), where ρ is the density of the elastomer and Vol the total geometrical volume of the actuator.

Figure 3.4. Show the amount of mass that is being moved at a particular time step.

$$m_{DEA_z} = \frac{z_{d(t)} - z_{d(t-1)}}{z_T} \rho Vol \quad (3.5)$$

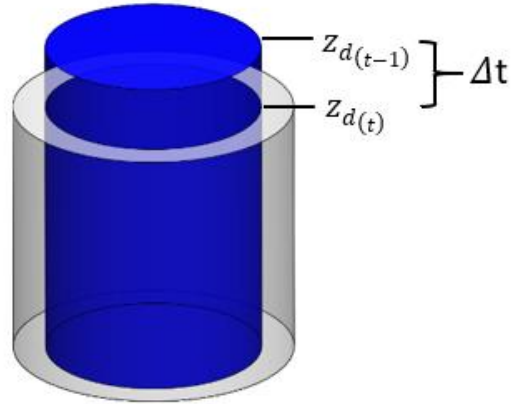


Figure 3.4. The amount of actuator mass being accelerated over time.

Notice that Equation (3.4) can also be represented in terms of acting pressure (3.6) by factorizing the surface area A_e of the electrodes that creates the electrostatic pressure

(3.8), which in case of cylindrical shaped DEA, the area of a circle is used (3.7); meanwhile, parametric areas for more complex geometries are also reported in literature (D. Kim, El Atrache, et al., 2019).

$$F_{load_z} - (\sigma_{el_z} - \sigma_{elast_z} - \sigma_{vis_z} - \sigma_{MW_z}) A_e = M_T \Delta \ddot{z} \quad (3.6)$$

$$F_{el_z} = \sigma_{el_z} A_e \quad (3.7)$$

$$A_e = \pi r^2 \quad (3.8)$$

The load force F_{load_z} (3.9) is create by the total mass M_T that is being pulled by gravity. M_T is the summation of the attached mass and a portion of the actuator mass, is this case it is assumed that at least half of the total mass of the actuator is being accelerate by gravity $g = 9.81 \text{ m/s}^2$ (3.10).

$$F_{load_z} = M_T g \quad (3.9)$$

$$M_T = m_{DEA}/2 + m_{load_z} \quad (3.10)$$

The first spring in parallel $f(\lambda_r, \lambda_z)$ in *Figure 3.3* (b) represents the nonlinear elastic functionality of the elastomeric material. Using models for hyperelasticity, the Cauchy stress σ_{elast_z} that governs the elastic deformation of $f(\lambda_r, \lambda_z)$ can obtained as shown in

equation (10). Notice that σ_{elast_z} depends on the chosen strain energy function W that best describe the S shape curve of the elastomer (Ali et al., 2010), and the volumetric hydrostatic pressure P from the boundary condition that affects its internal deformation (Lai & Tan, 2016). Finally, the stretches λ_z (3.11) and λ_r (3.12) denote the ratio of deformation in the principal directions of study within the material.

$$\sigma_{elast_z} = \lambda_z \frac{\partial W(\lambda_r, \lambda_z)}{\partial \lambda_z} - P = \frac{F_{elast_z}}{A_e} \quad (3.11)$$

$$\lambda_z = \frac{z_d(t)}{z_{d_0}} \quad (3.12)$$

$$\lambda_r = \frac{r(t)}{r_0} \quad (3.13)$$

The transient deformation of the elastomeric film is introduced by employing the generalize Kelvin-Maxwell model of viscoelasticity. The generalized Kelvin-Maxwell model is a combination of the Kelvin-Voight and Maxwell models (J. Zhang, Ru, et al., 2017) as shown in Figure 3.3 (b). The Kelvin-Voight model has embedded the hyperplastic spring $f(\lambda_r, \lambda_z)$ to model the nonlinear isostatic deformation of the

elastomer and a dashpot N_v that account for the deformation due to viscous losses under constant stress (3.13).

$$\sigma_{vis_z} = N_v \frac{\dot{z}_{d_0}}{z_{d_0}} = \frac{F_{vis_z}}{A_e} \quad (3.14)$$

Meanwhile, the Maxwell model aims to represent the complex stress relaxation reaction of the elastomeric material, notice that incrementing the number of elements in parallel in the Maxwell model proportionally contribute to accurate characterize more complex nonlinear relaxation effects (Serra-Aguila et al., 2019). The total relaxation stress is computed by the total summation of stresses from each parallel branches in the Maxwell model (3.14). Stresses from each Maxwell arm can be computed by Maxwell stress differential equation for viscous material (3.15).

$$\sigma_{MW_z} = \sum_{j=1}^{N_{MW}} \sigma_{MW_{z_j}} \quad (3.15)$$

$$\dot{\sigma}_{MW_z} = \left[k_j \frac{\dot{z}}{z_{d_0}} - \frac{k_j}{n_j} \sigma_{MW_z} \right] = \frac{F_{MW_z}}{A_e} \quad (3.16)$$

Finally, similar steps can be taken to find dynamics in the radial direction of the actuator. The summation of forces in the radial direction leads to differential Equation (3.17) by using free body diagram and lumped parameter models presented in Figure 3.5. The mass

m_{DEA_r} represents the total mass of the actuator that is being displaced on the radial direction which is equal to m_{DEA_z} and $\Delta\ddot{R}$ is that rate of acceleration in the radial direction.

$$\sum F_r: (\sigma_{elast_R} + \sigma_{vis_R} + \sigma_{MW_R})A_r = m_{DEA_r}\ddot{\Delta r} = F_R \quad (3.17)$$

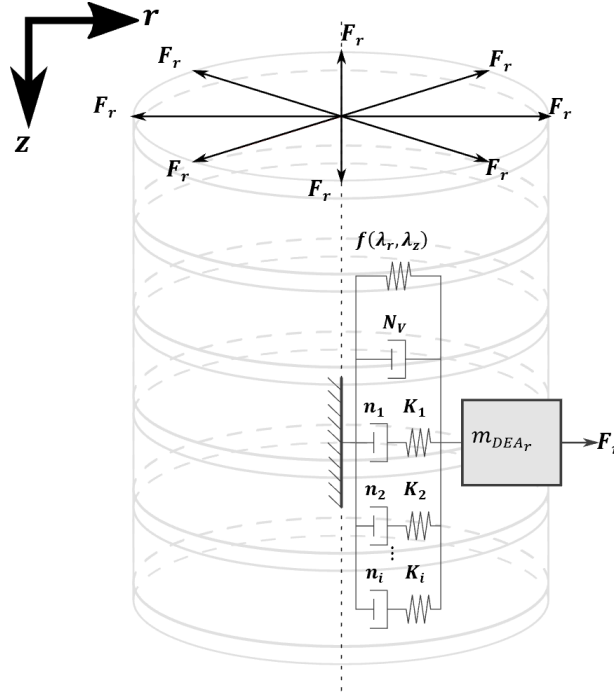


Figure 3.5. Free body diagram and lumped parameters in the radial axis.

Notice that no electrostatic forces or forces due to attached loads are considered in the sum of forces in the radial direction. The internal stresses due to incompressibility of the material lead to deformation of the radial deformation. There is an equivalent non-linear spring that represent the static hyperelastic relation between stress and strain in the radial

direction $f(\lambda_r, \lambda_z)$ (Figure 3.5.). Notice that σ_{elast_R} is the stress that deforms $f(\lambda_r, \lambda_z)$ and depends of the hydrostatic pressure P . Differential Equations (3.4) and (3.17) can be equated by using the hydrostatic pressure P ; thus, creating a connection between the z-axis and the radial axis dynamics.

$$\sigma_{\text{elast}_R} = \lambda_R \frac{\partial W}{\partial \lambda_R} - P \quad (3.18)$$

Transient response due to creep and relaxation also occurs on the radial direction, Equations (3.20), (3.21), and (3.22) solve for the Kelvin-Maxwell model of viscosity in the radial direction.

$$\sigma_{\text{vis}_z} = N_v \frac{\dot{r}(t)}{r_0} = \frac{F_{\text{vis}_r}}{A_r} \quad (3.19)$$

$$\sigma_{\text{MW}_r} = \sum_{j=1}^{N_{\text{MW}}} \sigma_{\text{MW}_{r_j}} \quad (3.20)$$

$$\dot{\sigma}_{\text{MW}_r} = \left[k_j \frac{\dot{r}}{r_0} - \frac{k_j}{n_j} \sigma_{\text{MW}_r} \right] = \frac{F_{\text{MW}_r}}{A_r} \quad (3.21)$$

The total electromechanical coupling between dynamics in the z-axis and radial direction is presented in an opened loop diagram presented in Figure 3.6.

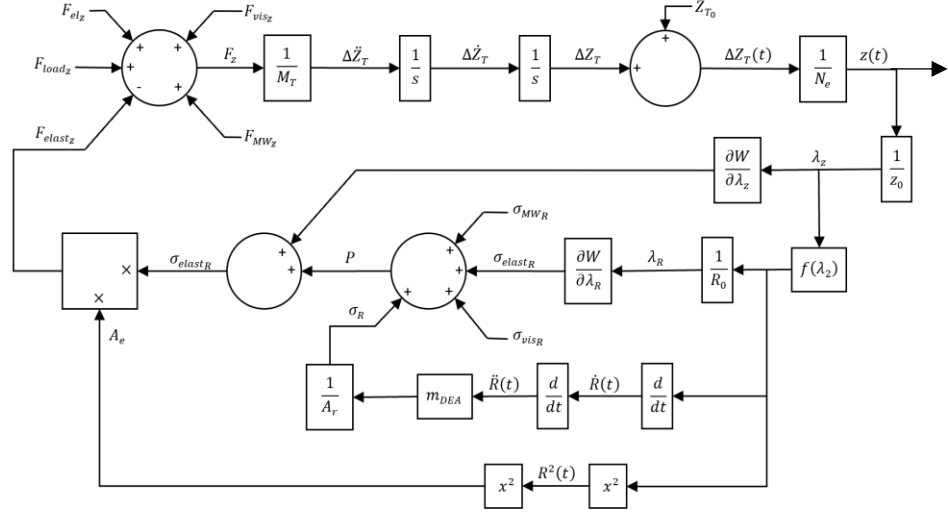


Figure 3.6. Open loop dynamics of multilayer DEA.

3.3 SELF SENSING

Dielectric elastomers can be represented as compliant capacitors that change their capacitance as the material change its shape. The equivalent electric circuit of a DEA can be understood by using a lumped parameter analogy as represented in *Figure 3.7*, where $C_{DEA}(\lambda_r, \lambda_z)$ is an electrical compliant capacitor, $R_D(\lambda_r, \lambda_z)$ is a varying resistance, and R_L is the resistance created by the wires. In this study, for simplicity $R_D(\lambda_r, \lambda_z)$ and R_L are neglected, since $R_D(\lambda_r, \lambda_z)$ is usually inversely proportional to C_{DEA} and R_L is very small. Chapter 4 develops further the electrical domain modeling of multilayer DEAs by introducing resistances and calculating power consumption.

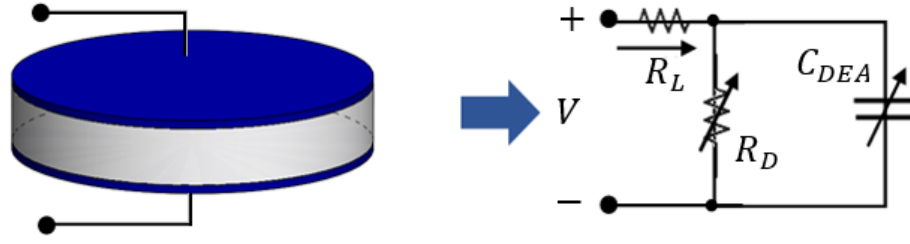


Figure 3.7. (a) Single DEA “Compliant capacitor”, (b) Equivalent circuit lumped parameter model.

The actuator is assumed to behave as an idea compliant capacitor and the self-sensing feature to come only from the change in capacitance, which can be calculated as follow:

$$C_{DEA}(\lambda_r, \lambda_z) = \frac{\epsilon_r \epsilon_0 A_e}{z_d} N_d \quad (3.22)$$

3.4 THE ACTUATOR AND FEM

The framework actuator consists of a multilayer DEA with circular cross section. The analytical model is constructed in MATLAB Simulink with an equivalent model in COMSOL Multiphysics® for numerical analysis. The elastomeric layers are characterized with materials parameters from the commercially available VHB4910 3M and no pre-stretch is applied to the model.

Table 3.1. *Initial condition for geometry of the cylindrical multilayer DEA*

Name	Value	Variable
Electrode radius [μm]	2250	r
Elastomer thickness [μm]	500	z_d
Electrode thickness [μm]	50	z_e
Electrode area [m^2]	1.5904e-05	A_e
Radial area [m^2]	7.0685e-05	A_r
Elastomer layers	10	n_d
Electrode layers	11	n_e

The acrylic VHB4910 is described as a soft elastomer that can undergo large deformation and whose behavior has been reported and approximately characterized by using the Yeoh strain energy function “ W ” of hyperelasticity (3.22) (Wissler & Mazza, 2005a).

$$W = \sum_{i=1}^3 c_{i0} (\bar{I}_1 - 3)^i \quad (3.23)$$

I_1 represents the first deviatoric strain invariant and can be calculated by means of the principal stretch ratios λ_x, λ_y and λ_z (3.24). In case of a cylindrical DEA, the longitudinal

orientation of the actuator match the z-axis (Figure 3); thus, the compression due to electrostatic pressure makes the material stretch along the z-axis (λ_z) leading to equally stretch in the in-plane direction λ_x and λ_y due to incompressibility, notice that $\lambda_x = \lambda_y = \lambda_r$. Finally, the assumption of material incompressibility defines that there is no change in volume and thus isochoric deformation occurs. Therefore, the product of its principal stretches should be constant and equal to one (3.25) which lead to the helping equation (3.26) for a relationship between λ_z and λ_r .

$$I_1 = \lambda_x^2 + \lambda_y^2 + \lambda_z^2 = 2\lambda_r^2 + \lambda_z^2 \quad (3.24)$$

$$\frac{Volume(t)}{Volume_0} = \lambda_r^2 \lambda_z = 1 \quad (3.25)$$

$$\lambda_z = \frac{1}{\lambda_r^2} \quad (3.26)$$

Table 3.2. *Material parameters for VHB4910 for Yeoh model.*

Parameter	Value
C10 [MPa]	0.0693
C20 [MPa]	$-8.88 * 10^{-4}$
C30 [MPa]	$16.7 * 10^{-6}$

The material constants of VHB4910 appears normalized in the literature as time relaxation and energy factor for Prony series modeling(Wissler & Mazza, 2007c) as shown in Table 3.3 The constants for the equivalent Kelvin-Maxwell model of

viscoelasticity can be computer by using the relationship between relaxation time and the spring and dashpot constants. of the lumped elements that compose the viscoelasticity model(Serra-Aguila et al., 2019), where $k_j/n_j = 1/\tau_i$, being τ is the relaxation time. The value of k_j are equal to g_j in table 3.3, and the first dashpot of the system N_v is taking in consideration if the material has some liquid behavior; thus, it is a value near zero for this case.

Table 3.3. *Viscoelastic parameters of VHB4910 for Yeoh model.*

Parameter	Value
N_v [MPa]	0
τ_1 [s]	0.153
g_1 [MPa]	0.478
τ_2 [s]	0.464
g_2 [MPa]	0.205
τ_3 [s]	32.021
g_3 [MPa]	0.0727
τ_4 [s]	215.85
g_4 [MPa]	0.0492

Table 3.4. *Complementary mechanical and electrical materials parameter of VHB4910 and actuator design.*

Parameter	Value	Variable
Relative Permittivity [-]	4.7	ϵ_r
Density [kg/m^3] (3M Inc., 2018)	960	ρ
Young's modulus [kPa] (Xu et al., 2015)	220	Y_o
Resistivity [$\Omega \cdot \text{m}$]	$3.1 * 10^8$	ρ_e

A multilayer DEA with the same geometry as shown in table 3.1 is modeled in the commercial software COMSOL Multiphysics® by utilizing the electromechanics simulation within MEMS module. The electromechanics function couples the nonlinear structural mechanics representing the hyperelasticity of the material and the viscous transient dynamics of the elastomer with the electrostatics Maxwell equations for pressure; therefore, once a voltage is applied within the electrical domain, the material is deformed because of the coupling. Figure 3.8 shows the modeling of the multilayer actuator and the mesh built. The mesh contains a number of 5706 domain elements and 1010 boundary elements. Figure 3.9 shows how to set up the numerical simulation in

COMSOL Multiphysics. Boundary conditions are imposed on the governing equations. The software solves the Maxwell electrostatic pressure equation (3.27) in three-dimensional space, which provides a more realistic scenario in comparison with the analytical model. Furthermore, because this simulation is set up as an axisymmetric, the results will come out as a three-dimensional space and are later be compared with the analytical model, which is design in one-dimensional space. Equation (3.27) is presented in symbolic form where E is the electric field tensor, I the identity tensor, and σ the Maxwell electrostatic stress tensor.

$$\sigma = \varepsilon_0 E \otimes E - \frac{1}{2} \varepsilon_0 (E \cdot E) I \quad (3.27)$$

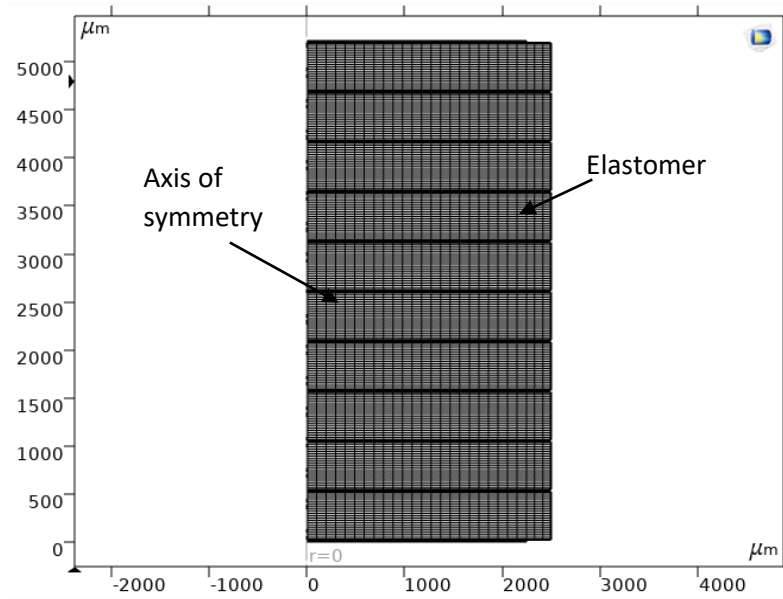


Figure 3.8. Mesh and multilayer DEA actuator (axisymmetric).

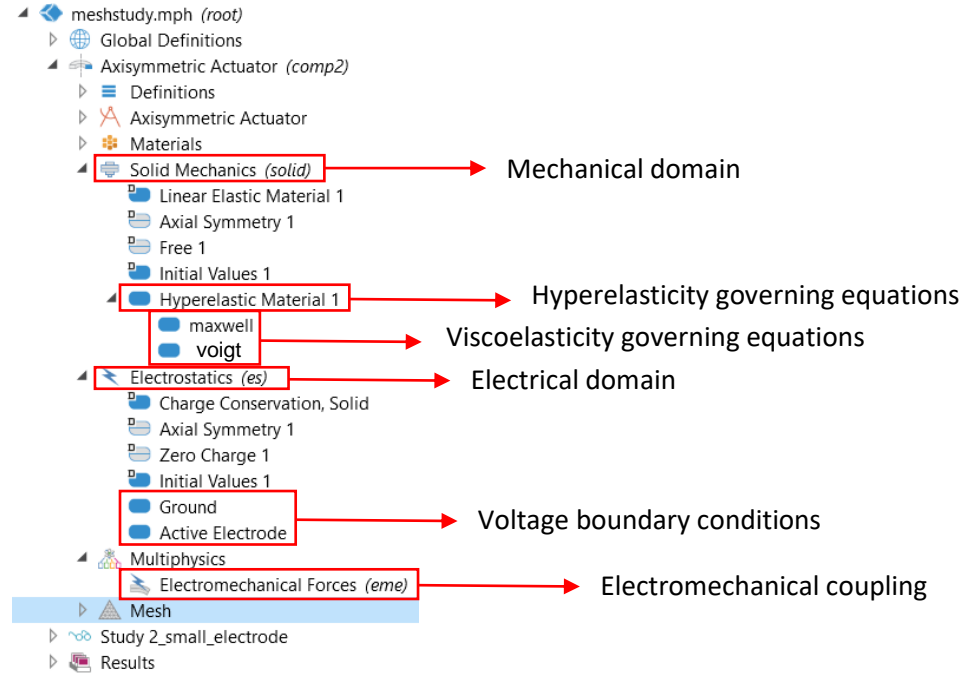


Figure 3.9. COMSOL Multiphysics model builder set up.

3.5 RESULTS

Data obtained from the numerical simulation in COMSOL Multiphysics is compared with the analytical solution from the one-dimensional dynamic equations preprogrammed in MATLAB/Simulink. The results from Figure 3.10. compares the transient response from analytical and numerical models. The actuator is excited with different constant voltages inputs (3 kV, 4 kV, 5 kV). The initial peak in the trajectory of the actuator is due to isostatic deformation while the transient deformation is due to viscous losses. The percentage of RMSE error can be computed by using equation (3.28) works as metric to measure the similitudes of the analytical response with respect the numerical results.

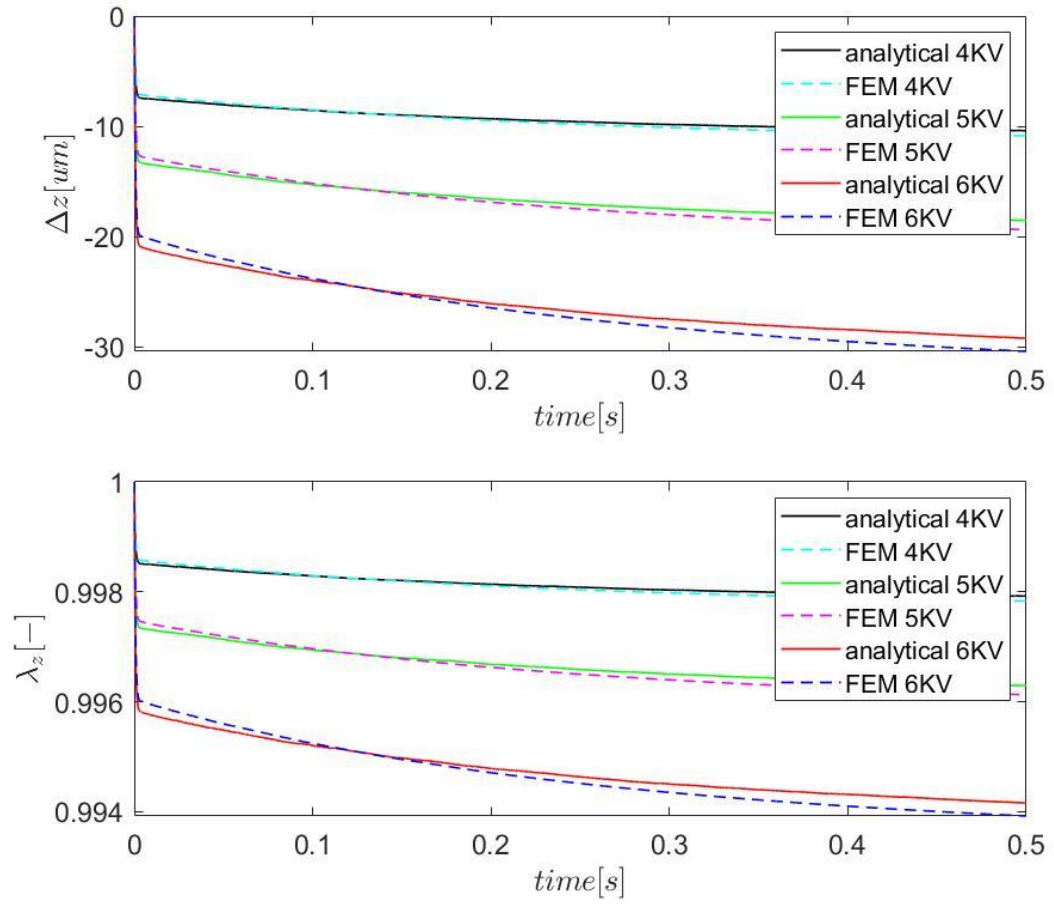


Figure 3.10. Comparison from analytical and numerical models.

$$\%RMSE = \frac{\sqrt{\sum_{i=1}^n \frac{(\hat{y}_i - y_i)^2}{n}}}{\max \hat{y}_i - \min \hat{y}_i} * 100 \quad (3.28)$$

Table 3.5. *Percentage of RSME error between analytical and FEM models at step input voltages*

Analytical Vs. FEM	RSME [%]
3 [kV]	2.55
4 [kV]	2.73
5 [kV]	2.49

The following graphs shows the behavior of the elastomeric actuator when under cyclical actuation. The first element to notice is the hysteresis presented after each cycle; this is due to viscous losses, which tend to keep deforming the material over time. The actuator is excited with a triangle wave with five peaks and at different frequencies. The error is computed through the %*RMSE* (3.28) (Table 3.6) over five cycles for 10Hz and 50Hz and 100Hz.

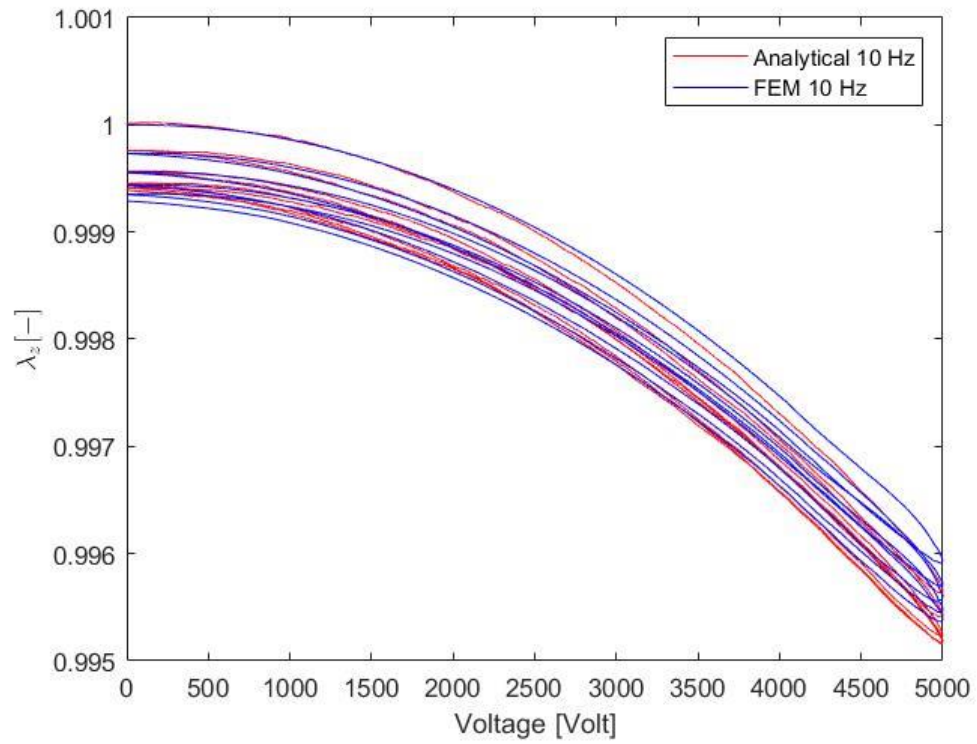


Figure 3.11. Actuator displacement under 10 Hz cyclic voltage input demonstrating hysteresis.

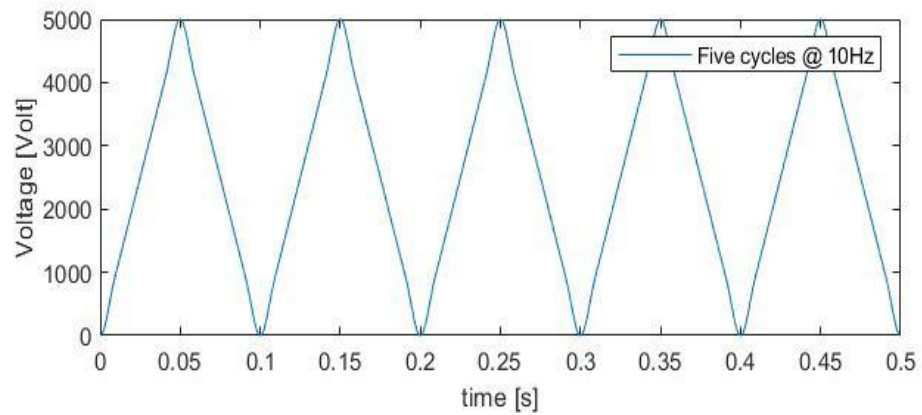


Figure 3.12. Voltage input for Figure 3.11.

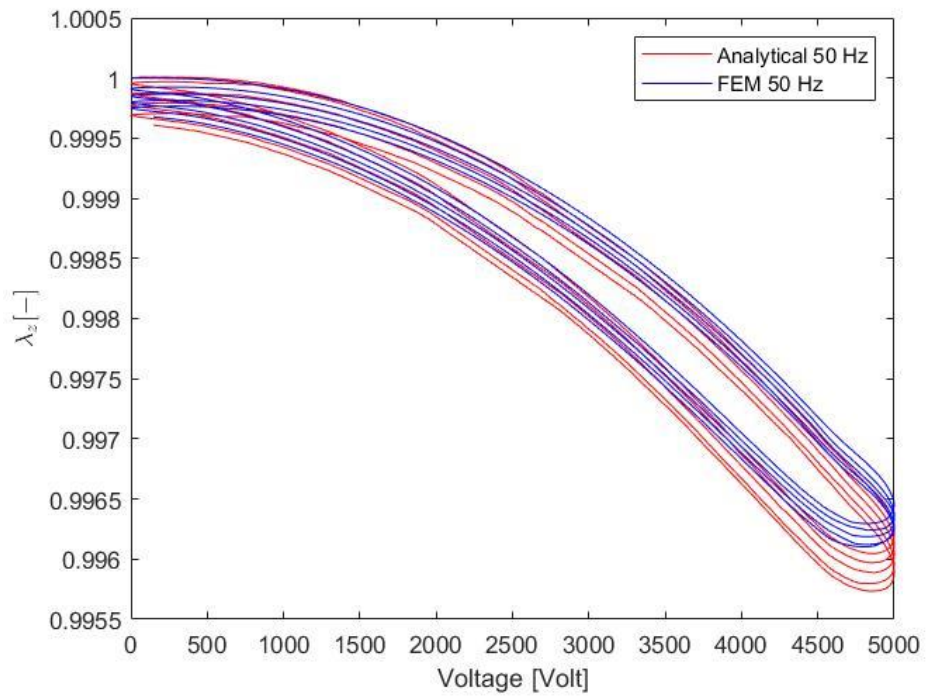


Figure 3.13. Actuator displacement under 50 Hz cyclic voltage input demonstrating hysteresis.

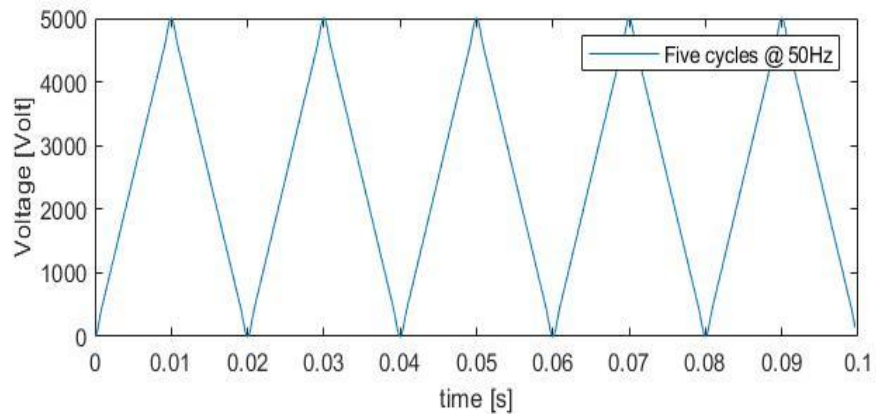


Figure 3.14. Voltage input for Figure 3.13.

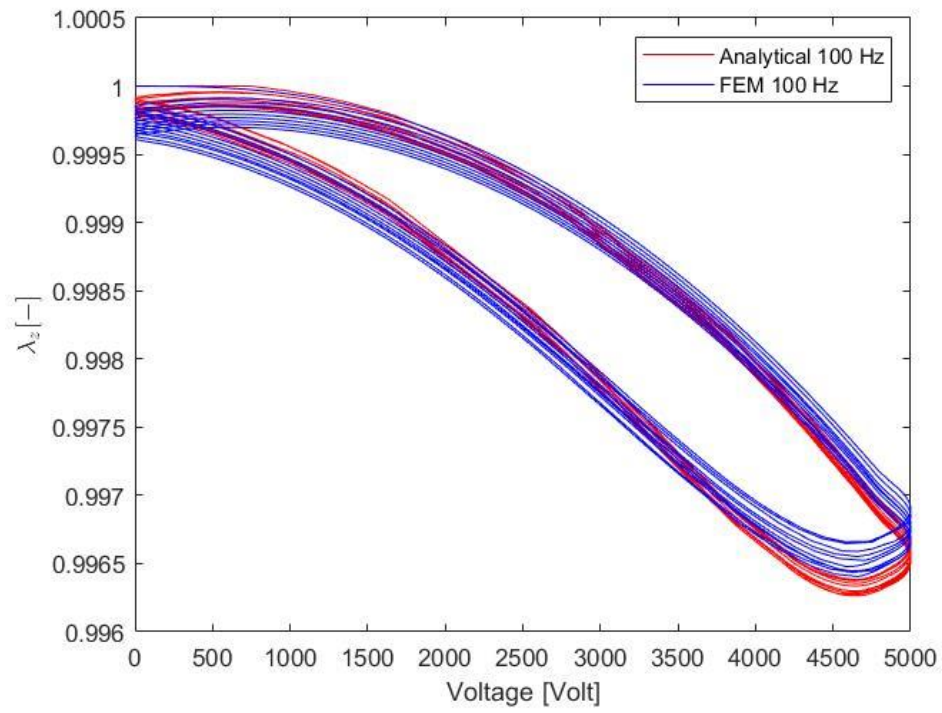


Figure 3.15. Actuator displacement under 100 Hz cyclic voltage input demonstrating hysteresis.

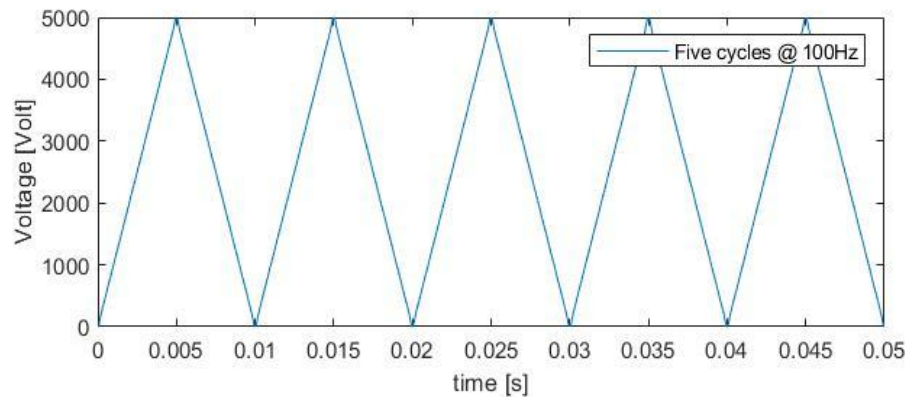


Figure 3.16. Voltage input for Figure 3.11.

Table 3.6. Percentage of RSME error between analytical and FEM models from triangle wave input voltages

Analytical Vs. FEM	RSME [%]
10 [Hz]	2.55
50 [Hz]	3.15
100 [Hz]	2.90

3.6 Control systems

One of the purposes of having a proper dynamic model is for the testing of control systems. As shown in Figure 3.17 the dynamic model presented in this research is used to test a PID controller (3.29). It can be notice that the error between the trajectory and the actual position is high. This is due because the nonlinearity of the system. However, the key error to take in consideration is that the actuator response is monotonically decreasing over time because of viscoelasticity and changes in the rate of deformation. The % RSME error was 15.21% and it can be hypothesized that it will increase over time because the viscous loses in the system.

$$u = K_p e + K_i \int_0^t e dt + K_d \frac{d}{dt} e \quad (3.29)$$

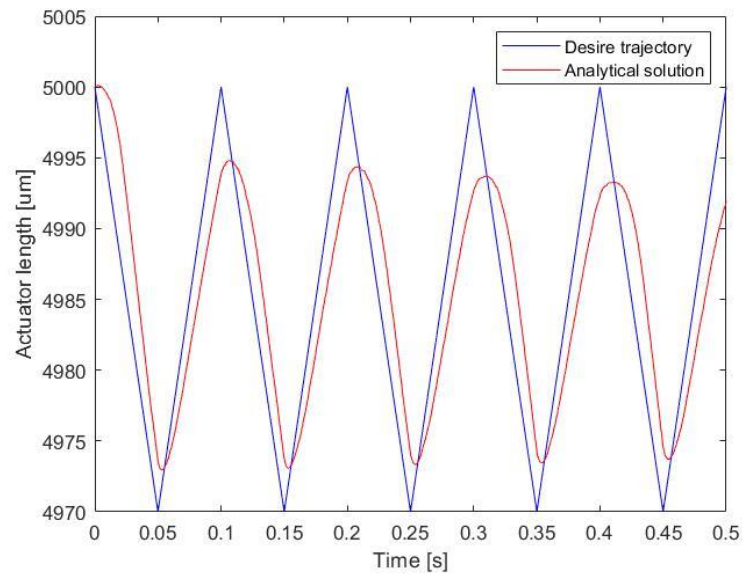


Figure 3.17. PID tracking a triangle wave trajectory.

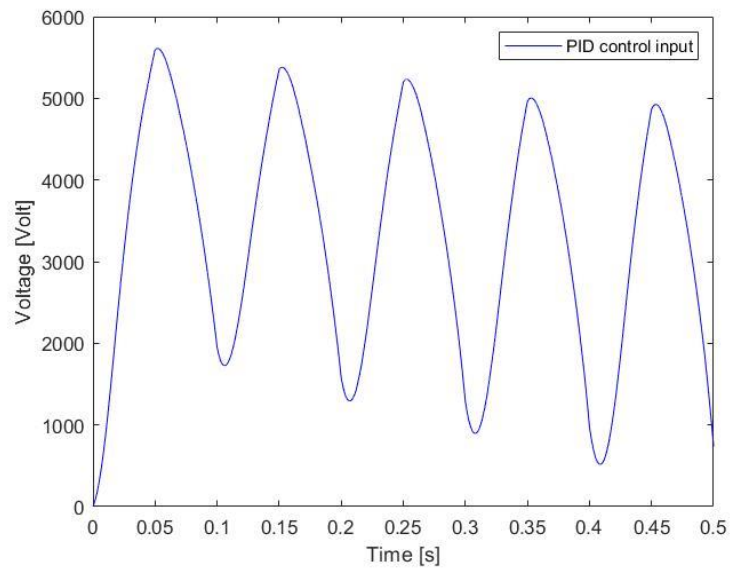


Figure 3.18. PID command output.

The change in the capacitance while the actuator is tracking a triangle wave is shown in (Figure 3.19). It can be notice that the capacitance is inversely proportional to the thickness of the elastomer (Figure 3.17). The measure of the capacitance can be used as a self-sensing mechanism to estimate the current position of the actuator.

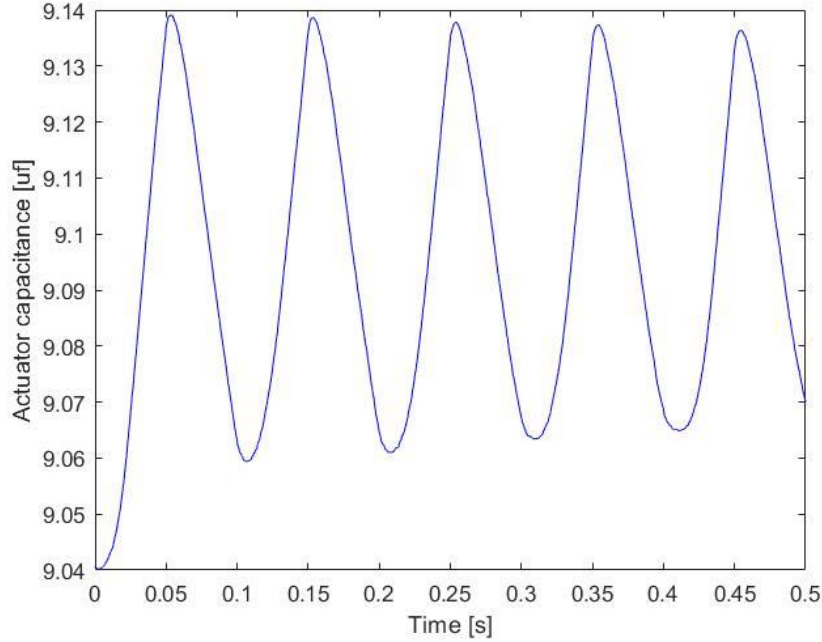


Figure 3.19. Actuator capacitance while tracking the triangle trajectory.

3.7 CONCLUSIONS

The methodology presented in this work aims for the derivation of dynamic models for multilayer DEAs. The study compared the results from analytical and numerical model and provide close results with an RSME% error of around 2.5%.

This small error can be hypothesize from different factors. First, the proposed analytical

model is derived using one-dimensional equations while the numerical model is tridimensional. Second, the inertial mass displaced at time of deformation is assumed half of the total mass of the actor, which in practicality is not the case. Furthermore, using equation 3.5 to estimate the amount of mass that is being displaced when the elastomer is deforming needs an initial guess because the actuator first needs an initial input voltage to know how much is going to be compressed.

The application of a PID controller proved that the model could be used to test control systems. The controller proved to be inadequate for this task because of the nonlinearity of the system plus the viscous losses; thus, making the PID to hardly track a desired trajectory. Future studies could use more advanced learning algorithms in order to decrease the tracking error such as reinforcement learning.

Chapter 4 A dynamic model of helical dielectric elastomer actuator

4.1 Introduction

This chapter utilizes the methodology presented in chapter 3 of using lumped parameters to model the dynamical system and power consumption of a helical dielectric elastomer actuator (HDEA). The HDEA is a novel type of DEA with an attractive continuous structure where electrodes are embedded and interrupted through the whole device. This design is more attractive than regular multi-layer DEA where all electrodes need to be connected in parallel. Meanwhile, this is a special geometrical configuration requires a parametrization of its geometry that couples with the equations of hyperelasticity which elevates the complexity and nonlinearity of the system.

4.2 HDEA geometrical structure

The complex geometrical structure of the HDEA have been well developed in previous research (Gbaguidi et al., 2016). It is constructed principally by the pitch of the helix which is define by the number of elastomeric elements N_e in series in one period and the thickness of each elastomer $z(t)$.

$$Pitch = N_e z(t) \quad (4.1)$$

Furthermore, the total height of the actuator $Z_T(t)$ can be computed by multiplying the time varying pitch of the helix times the number of periods N_p defined designed

morphology of the actuator.

$$Z_T(t) = P(t) N_p \quad (4.2)$$

It is important to mention that the electrostatic forces act in a direction that is perpendicular to the electrodes that are compressing the material. Thus, the distance between two electrodes in a helical system can be defined as:

$$h(t) = z(t) \sin \alpha(t) \quad (4.3)$$

Where $\alpha(t)$ is defined as complementary inclination angle of the elastomer. As this angle approaches $\pi/2$, the intensity of the electrostatic forces increases towards the z direction (Carpi & de Rossi, 2012).

$$\alpha(t) = \arctan \left(\frac{4 R_o}{P(t)} \right) \quad (4.4)$$

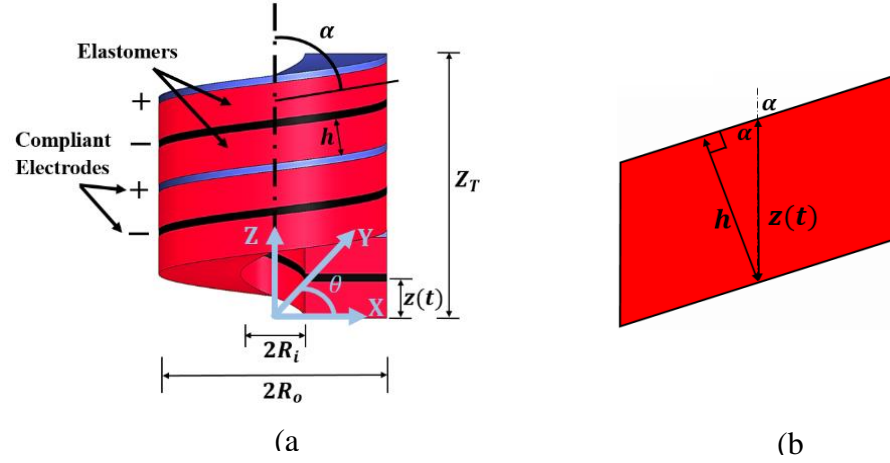


Figure 4.1. (a) Shows the HDEA geometrical structure, (b) shows the relation of the thickness $z(t)$ of the elastomer and the electrode distance $h(t)$ by using the complementary angle $\alpha(t)$.

It can be observed that the HDEA is trapped into a cylindrical coordinasystem where any particle in the helix can be parametrically characterized in the cartesian coordinate system.

$$\phi(r, \theta) = \begin{cases} x = r \cos \theta \\ y = r \sin \theta \\ z = c \theta \end{cases} \quad (4.5)$$

Where c is the slant of the helix and when assuming one period ($N_p = 1$), the azimuth angle θ is equal to 2π ; thus, the slant becomes $c = \text{Pitch}/2\pi$. Furthermore, the length of helical curve of one period of helix can be calculated taking the following steps (Gbaguidi et al., 2016).

Taking a partial derivate of the parametric vector $\phi(r, \theta)$ with respect to the variable radius r .

$$\frac{\partial \phi}{\partial \theta}(r, \theta) = \begin{cases} dx = -r \sin \theta d\theta \\ dy = r \cos \theta d\theta \\ dz = c d\theta \end{cases} \quad (4.6)$$

Calculating the infinitesimal arc length of the curve as:

$$\begin{aligned} dL &= \sqrt{(dx)^2 + (dy)^2 + (dz)^2} = \sqrt{(-r \sin \theta)^2 + (r \cos \theta)^2 + (c)^2} d\theta \\ &= \sqrt{r^2 + c^2} d\theta. \end{aligned} \quad (4.7)$$

Finally, the length of a helical curve at any radius r and bounded by one helical period is calculated as following:

$$L_r = \int dL = L_r = \int_0^{2\pi} \sqrt{r^2 + c^2} d\theta = 2\pi \sqrt{r^2 + c^2} \quad (4.8)$$

In addition, the surface area of an elastomer that is bounded in one helical period can be compute as:

$$A = \iint \left\| \frac{\partial \phi}{\partial r}(r, \theta) \times \frac{\partial \phi}{\partial \theta}(r, \theta) \right\| dr d\theta \quad (4.9)$$

Where

$$\left\| \frac{\partial \phi}{\partial r}(r, \theta) \times \frac{\partial \phi}{\partial \theta}(r, \theta) \right\| = \sqrt{(c \sin \theta)^2 + (-c \cos \theta)^2 + (r)^2} = \sqrt{r^2 + c^2} \quad (4.10)$$

To continue, for one helical period the surface area will be bounded by the radius $R_i < r < R_o$ and can be computed as:

$$A_{R_i R_o} = \iint \sqrt{r^2 + c^2} dr d\theta = \int_0^{2\pi} \int_{R_i}^{R_o} \sqrt{r^2 + c^2} dr d\theta \quad (4.11)$$

Finally, the integration gives:

$$A_e(t) = A_{R_i R_o} = \pi \left[R_o(t) \sqrt{R_o(t)^2 + c(t)^2} - R_i(t) \sqrt{R_i(t)^2 + c(t)^2} + c(t)^2 \ln \left(\frac{R_o(t) + \sqrt{R_o(t)^2 + c(t)^2}}{R_i(t) + \sqrt{R_i(t)^2 + c(t)^2}} \right) \right] \quad (4.12)$$

It is important to mention that the surface area of the elastomer will be the same as the electrodes surface area since they are considered compliant. Furthermore, other areas that comprise the geometry of the elastomer can be computed and are presented in Figure 4.2.

The elastomer cross section are $A_\theta(t)$ is:

$$A_\theta(t) = (R_o(t) - R_i(t)) z(t) \quad (4.13)$$

The external area of the elastomer $A_{rl_o}(t)$ and internal area of the elastomer $A_{rl_i}(t)$ are:

$$A_{rl_o}(t) = z(t)2\pi\sqrt{R_o(t)^2 + c^2} \quad (4.14)$$

$$A_{rl_i}(t) = z(t)2\pi\sqrt{R_i(t)^2 + c^2} \quad (4.15)$$

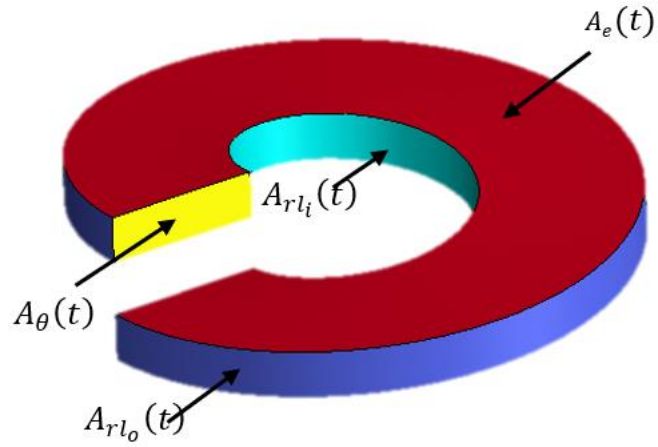


Figure 4.2. Representation of the areas that encloses the volume of a HDEA.

4.3 Principal stretches of the HEDA

The principal stretches are ratios denoting the amount of material stretch in the principal direction studied. These ratios directly relate to dimensions of interest for the HDEA geometry. Furthermore, they are used to calculate the principal invariants that compose the strain energy function of hyperelastic constitutive models.

The stretch ratio λ_z of the thickness of the material is given by Equation (4.16) where it is

also related to the thickness strain S_z .

$$\lambda_z = \frac{z(t)}{z_0} = \frac{z_0 - (z_0 - z(t))}{z_0} = 1 - S_z \quad (4.16)$$

The delta radial stretch ratio $\lambda_{\Delta r}$ is calculated by:

$$\lambda_{\Delta r} = \frac{R_o(t) - R_i(t)}{R_{o_0} - R_{i_0}} \quad (4.17)$$

Where $R_o(t) - R_i(t)$ is the change of the width of the elastomer with as function time and it is denoted as $\Delta R(t)$. Furthermore, it can be assumed that the amount of change in $R_o(t)$ is very close to the amount of change of $R_i(t)$. Thus, $R_i(t)$ can be computed.

$$R_i(t) = R_{i_0} + R_{o_0} - R_o(t) \quad (4.18)$$

The longitudinal stretch ratio of the length of the helical λ_{L_R} is depended by the radius used in its calculation since the HDEA has an inner and outer ratio. Therefore, Equation (4.19) is not the most appropriate way to calculate this principal stretch.

$$\lambda_{L_R} = \frac{L_r(t)}{L_{r_o}} \quad (4.19)$$

However, because it is assumed that the elastomer is incompressible, it will conserve its

volume through time. As a result, another path to compute λ_{LR} is presented. As shown in Equation (4.20) the rate of change of the volume will always be equal to one. Therefore, this simplification can lead to a relation between the initial and current elastomer thickness and area of the elastomer.

$$\frac{Vol(t)}{Vol_o} = \frac{A_e(t)z(t)}{A_{e_0}z_0} = 1 \quad (4.20)$$

By coupling equation (4.20) with equation (4.12) a relationship between the current $z(t)$ and $R_o(t)$ can be found by relating the electrode area at current time with the initial time. However, this equation needs a numerical technique to be solved. For simplicity, this equation will be presented and will appear in the open loop block diagram of the actuator as shown in Equation (4.21).

$$\left[R_o(t) \sqrt{R_o(t)^2 + \left(\frac{z(t)}{\pi}\right)^2} - (R_{i_0} + R_{o_0} - R_o(t)) \sqrt{(R_{i_0} + R_{o_0} - R_o(t))^2 + \left(\frac{z(t)}{\pi}\right)^2} \right. \\ \left. + \left(\frac{z(t)}{\pi}\right)^2 \ln \left(\frac{R_o(t) + \sqrt{R_o(t)^2 + \left(\frac{z(t)}{\pi}\right)^2}}{(R_{i_0} + R_{o_0} - R_o(t)) + \sqrt{(R_{i_0} + R_{o_0} - R_o(t))^2 + \left(\frac{z(t)}{\pi}\right)^2}} \right) \right] z(t) = \frac{A_0 z_0}{\pi}$$

$$R_o(t) = f(z(t), R_o(t)) \quad (4.21)$$

Finally, because an incompressible material has the following property $\lambda_{L_r}\lambda_{\Delta r}\lambda_z = 1$, the longitudinal stretch ratio λ_{L_r} can be computed as shown in Equation (4.22).

$$\lambda_{L_r} = \frac{1}{\lambda_{\Delta r}\lambda_z} \quad (4.22)$$

4.4 Free body diagrams and dynamics

The dynamic model of the HDEA is derived by using lumped parameters that equals the free body diagram of the system (Hodgins et al., 2014; Hoffstadt & Maas, 2015b). This lumped-parameter model is formed using different springs and dashpots that represent the hyperelastic and viscous responses of the mechanical system of the actuator.

Furthermore, it contains the external elements representing an intrinsic portion of actuator mass being deformed at the moment of actuation, the external affixed load, and the action of the electrostatic forces in the mechanical domain. As shown in Figure 4.3 (b), Figure 4.4 (a) from left to right, and Figure 4.5 (b) from top to bottom, the first two elements of the system in parallel represent the Kelvin-Voigt model of viscoelasticity, where the spring $f(\lambda_{L_r}, \lambda_{\Delta r}, \lambda_z)$ represent the hyperelastic resistance and the dashpot in parallel represents the viscous response with a viscosity coefficient N_V . Furthermore, the series of springs and dashpots connected in parallel represent the viscoelastic Maxwell model, where k_j and n_j are their respective coefficients. The additional N elements in parallel

ensure a more accurate simulated response of the viscous system. The combination of these two models of viscoelasticity together are known as the Generalized Kelvin-Maxwell Model (Fancello et al., 2006b). Furthermore, it is important to note that the elastomeric material is considered isotropic in this study; thus, the parametric constants of the springs and dashpots are equal in every direction of the material.

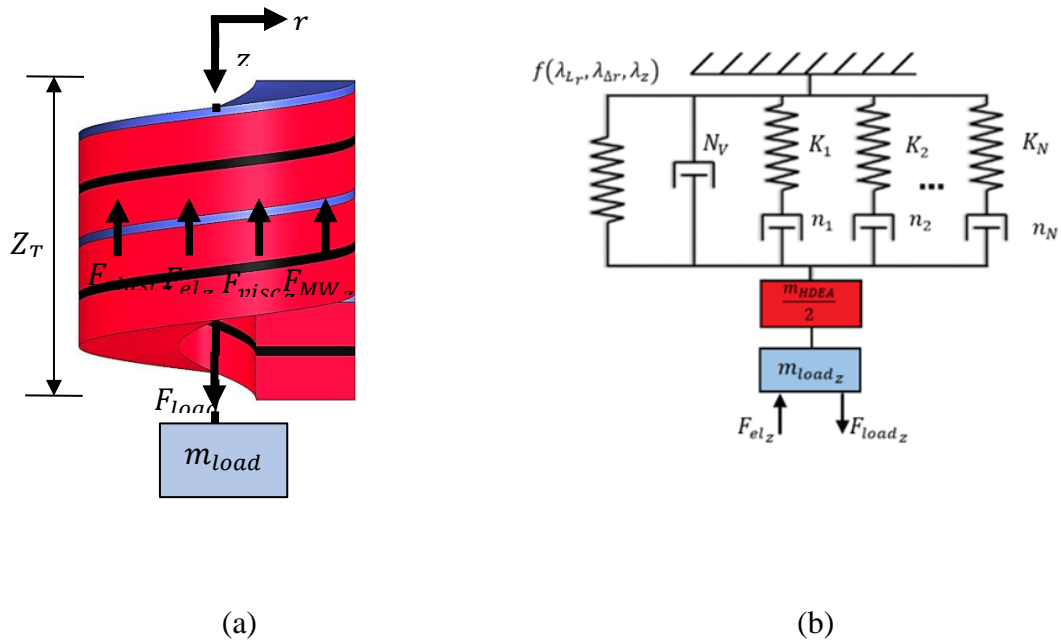


Figure 4.3. (a) Free body diagram of the forces in the z -axis, (b) Lumped parameter model in the z direction.

The summation of forces in the z -axis shown in Equation (4.23) can be derived from the

free body diagram presented in Figure 4.3.

$$\sum F_z: F_{load_z} - F_{el_z} - F_{H-elastic_z} - F_{vis_z} - F_{MW_z} = M_T \ddot{Z}_T \quad (4.23)$$

Where F_{el_z} characterizes the electrostatic force transferred in the z-direction can be obtained as shown in Equation (4.24) where σ_z is the electrostatic stress in the z-axis direction of a cylindrical coordinate system once σ_{el} in Equation (2.1) is multiplied by $\sin(\alpha)$ (Carpi & de Rossi, 2012).

$$F_{el_z} = \sigma_{el_z} A_e = \frac{\epsilon_r \epsilon_0 V^2}{z^2 \sin(\alpha)} A_e \quad (4.24)$$

The total load F_{load_z} that is being moved in the z-axis is calculated as:

$$F_{load_z} = M_T g \quad (4.25)$$

Where M_T is the total mas moved by the summation of the attached weight and the mass of the HDEA that is being displacement at the actuation time in the z-direction.

Furthermore, it can be noted that half of the mass of the HDEA is assumed to be moving (Hoffstadt & Maas, 2015b); therefore, $m_{HDEA_z} = m_{HDEA}/2$. Finally, gravity acting on the system is denoted by g , which is equal to 9.81 m/s^2 .

$$M_T = m_{HDEA_z} + m_{load_z} \quad (4.26)$$

$F_{H-elastic_z}$ represents the action force of the non-linear hyperelastic spring and can be compute as:

$$F_{H-elastic_z} = \sigma_{etalst_z} A_e \quad (4.27)$$

Where σ_{etalst_z} represent the Cauchy stress in the z-axis and is giving by:

$$\sigma_{etalst_z} = \lambda_z \frac{\partial W}{\partial \lambda_z} - P \quad (4.28)$$

The viscous force F_{vis_z} represents the damper response of the dashpot N_V from the kelvin-Voigt model and is derived to be:

$$F_{vis_z} = N_V \dot{z} \frac{A_e}{z_0} \quad (4.29)$$

Finally, the viscous force $F_{vis_{L_r}}$ exerted by the Maxwell model can be calculated as shown in Equation (4.30) from the summation of the N branches of elements in parallel. However, in order to solve for every $F_{MW_{z_j}}$, a differential equation has to be solved as shown in Equation (4.31).

$$F_{MW_z} = \sum_{j=1}^{N_{MW}} F_{MW_z j} \quad (4.30)$$

$$\dot{F}_{MW_z} = \left[k_j \dot{z} \frac{A_e}{z_0} - \frac{k_j}{n_j} F_{MZ_z} \right] \quad (4.31)$$

To continue, the summation of forces presented in Equation (4.32) that acts alongside the helical curve L_r are derived from the lumped parameter model shown below in the

Figure 4.4.

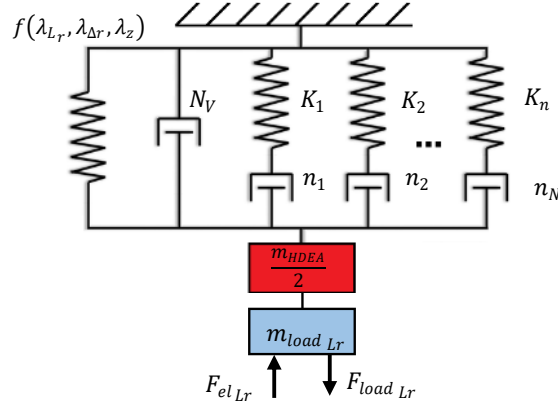


Figure 4.4. Lumped parameter model in the direction of the helical curve L_r .

$$\sum F_{L_r} : - F_{el_{L_r}} + F_{load_{L_r}} - F_{H-elast_{L_r}} - F_{vis_{L_r}} - F_{MW_{L_r}} = M_{T_{L_r}} \ddot{L_r} \quad (4.32)$$

The electrostatic force $F_{el_{L_r}}$ can be determined as shown in Equation (4.33) where σ_{L_r} is the electrostatic stress in the in cylindrical coordinate system once σ_{el} in Equation (2.1) is multiplied by $\cos(\alpha)$.

$$F_{el_{L_r}} = \sigma_{el_{L_r}} A_\theta = \frac{\varepsilon_r \varepsilon_o \cos(\alpha) V^2}{z^2 \sin(\alpha)^2} A_\theta \quad (4.33)$$

The total load represented by the force $F_{load_{L_r}}$ that affects around the helical curve is calculated as shown in Equation (4.34), where M_T is calculate with Equation (4.26) and g is the gravity.

$$F_{load_{L_r}} = F_{load} \cos(\alpha) = M_T g \cos(\alpha) \quad (4.34)$$

Furthermore, there will be a force $F_{H-elastic_{L_r}}$ representing the action of a non-linear hyperelastic spring through the helical curve L_r .

$$F_{H-elastic_{L_r}} = \sigma_{etalst_{L_r}} A_\theta \quad (4.35)$$

Where $\sigma_{etalst_{L_r}}$ represents the Cauchy stress through the helical curve L_r and is given by:

$$\sigma_{etalst_{L_r}} = \lambda_{L_r} \frac{\partial W}{\partial \lambda_{L_r}} - P \quad (4.36)$$

Furthermore, the viscous force reactions needed to complete the generalized Kelvin-Maxwell model (Fancello et al., 2006b) can be accounted for by using Equations (4.37), (4.38) and (4.39).

$$F_{vis_{Lr}} = N_E \dot{L}_r \frac{A_{Lr}}{L_{r0}} \quad (4.37)$$

$$F_{MW_{Lr}} = \sum_{j=1}^{N_{MW}} F_{MW_{Lrj}} \quad (4.38)$$

$$\dot{F}_{MW_{Lr}} = \left[k_j \dot{L}_r \frac{A_\theta}{L_{r0}} - \frac{k_j}{n_j} F_{MZ_{Lr}} \right] \quad (4.39)$$

Finally, using the lumped parameter system shown in Figure 4.5 the net force in the radial direction can be derived as shown in the Equation (4.40) where the mass $m_{HDEA_r} = m_{HDEA_z}(1 - \cos \alpha)$. Notice this derivation is executed with the intention of solving for the hydrostatic pressure P . This hydrostatic pressure can be substituted into Equations (4.28) and (4.36). Furthermore, because of the cylindrical coordinate system, no electrostatic pressure will appear in this direction (Carpi & de Rossi, 2012).

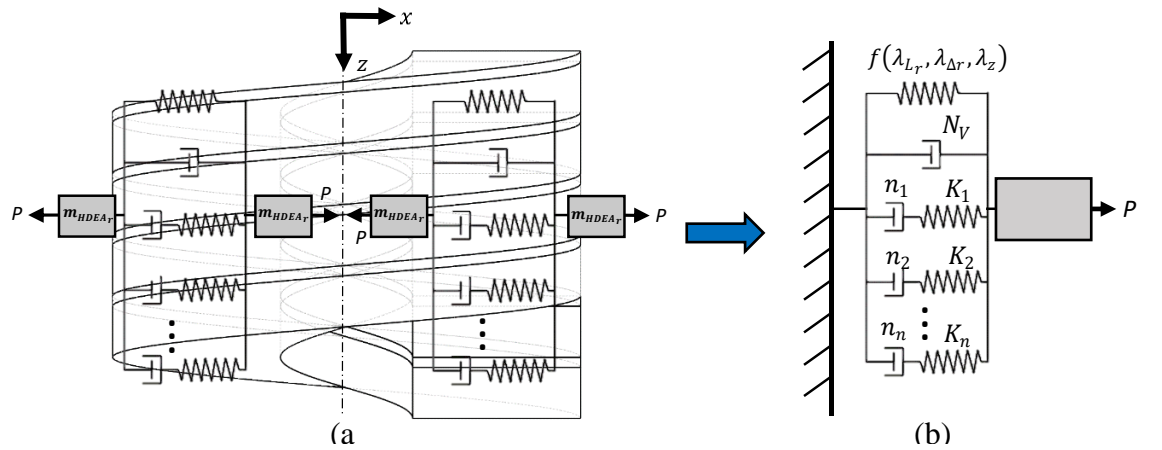


Figure 4.5. (a) 2D representation of the internal lumped parameter model of the mechanical reactions that causes the deformation of $\Delta R(t)$, (b) conservative simplification of the 2D model.

$$\sum F_{\Delta r}: F_{H-elastic_{\Delta r}} + F_{vis_{\Delta r}} + F_{MW_{\Delta r}} = m_{HDEA_r} \ddot{\Delta R} \quad (4.40)$$

To continue, as mentioned in the previous force derivation, the force $F_{H-elastic_{\Delta r}}$ shown in Equation (4.41) represents the action of a non-linear hyperelastic spring; however, this time is in the radial direction. Furthermore, Equation (4.42) shows how the force $F_{H-elastic_{\Delta r}}$ is dependent on hydrostatic pressure P .

$$F_{H-elastic_{\Delta r}} = \sigma_{elastic_{\Delta r}} A_{rl} \quad (4.41)$$

$$\sigma_{elastic_{\Delta r}} = \lambda_{\Delta r} \frac{\partial W}{\partial \lambda_{\Delta r}} - P \quad (4.42)$$

Furthermore, the additional viscous force reactions needed to complete the generalized Kelvin-Maxwell model can be found by using Equations (4.43), (4.44) and (4.45).

$$F_{vis_{\Delta r}} = N_V \dot{\Delta R} \frac{A_{rl}}{R_o - R_i} \quad (4.43)$$

$$F_{MW_{\Delta r}} = \sum_{j=1}^{N_{MW}} F_{MW_{\Delta r}j} \quad (4.44)$$

$$\dot{F}_{MW_{\Delta r}} = \left[k_j \dot{\Delta R} \frac{A_{rl}}{R_o - R_i} - \frac{k_j}{n_j} F_{MZ_{\Delta r}} \right] \quad (4.45)$$

Finally, the hydrostatic pressure can be solved as shown in Equation (4.46).

$$P = -\frac{m_{HDEA_r} \ddot{\Delta R}}{A_{rl}} + \lambda_{\Delta r} \frac{\partial W}{\partial \lambda_{\Delta r}} + N_v \frac{\dot{\Delta R}}{R_o - R_i} + \frac{F_{MW_{\Delta r}}}{A_{rl}} \quad (4.46)$$

4.5 Power consumption

The power consumption of the HDEA can be understood by using a lumped parameter analogy (Hackl et al., 2005; Hoffstadt & Maas, 2015b) as represented in figure 3.6, where $C_{HDEA}(\lambda_{L_r}, \lambda_{\Delta r}, \lambda_z)$ is an electrical compliant capacitor, $R_D(\lambda_{L_r}, \lambda_{\Delta r}, \lambda_z)$ is a varying resistance, and R_L is the resistance created by the wires, which this study neglects since it is usually very small.

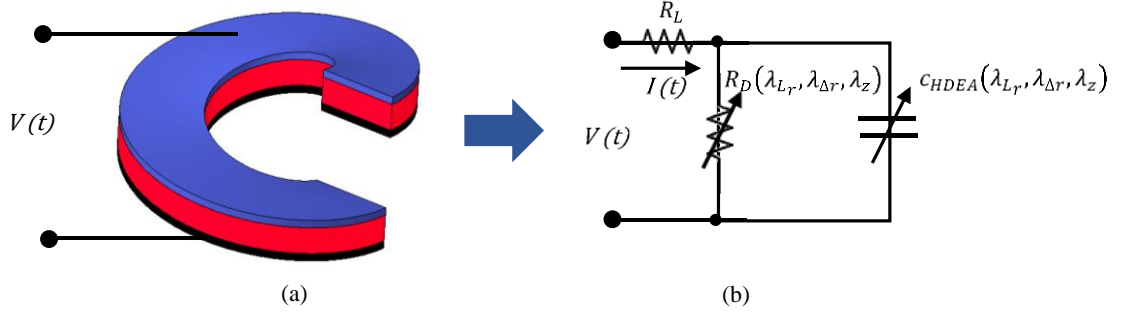


Figure 4.6. (a) HDEA with voltage applied by connecting wires to the actuator, (b) Lumped parameter analogy of the electrical system of the HDEA.

The electrical compliant capacitance can be calculated as:

$$C_{HDEA}(\lambda_{Lr}, \lambda_{\Delta r}, \lambda_z) = \frac{\epsilon_r \epsilon_o A_e(t)}{h(t)} N_p N_e \quad (4.47)$$

The varying resistance $R_D(\lambda_{Lr}, \lambda_{\Delta r}, \lambda_z)$ can be represented by:

$$R_D(\lambda_{Lr}, \lambda_{\Delta r}, \lambda_z) = \frac{\rho h(t)}{A_e(t) N_p} N_e \quad (4.48)$$

Where ρ is the electrical resistivity of the elastomer material. Furthermore, it can be found in the literature that this parameter changes depending on the pre-stretch applied to the DEA and the amount of electric field that is applied (Barnes et al., 2007).

Therefore, the total current $I(t)$ coming into the system can be calculated as shown in Equation (4.49).

$$I(t) = \frac{V(t)}{R_D(\lambda_{Lr}, \lambda_{\Delta r}, \lambda_z)} + C_{HDEA}(\lambda_{Lr}, \lambda_{\Delta r}, \lambda_z) \frac{dV(t)}{dt} \quad (4.49)$$

Finally, the electrical power consumption can be derived, demonstrated in Equation (4.50).

$$Power_{el} = V(t) I(t) \quad (4.50)$$

Block diagram of the open loop response of the HDEA

The complete electromechanical coupling that shows the open loop response of the HDEA can be found in Figure 4.7, where also it can be noticed that the only input to the system is the voltage $V(t)$ and the output are the current states of the morphology of the actuator and kinematics. The block diagram shown in Figure 4.8 has also subsystems that form part of the main system.

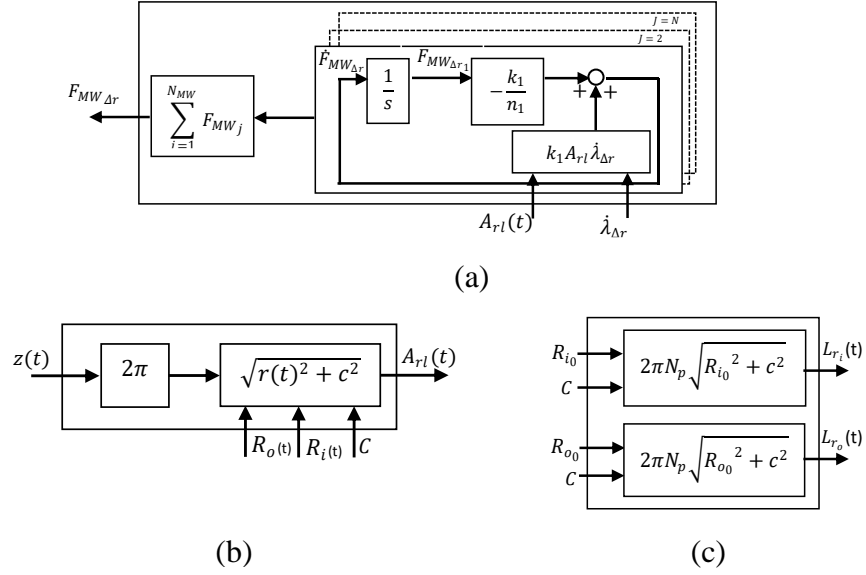


Figure 4.8. (a) Sub-System A of the open loop response in Figure 4.7, (b) Sub-System B of the open loop response in Figure 4.7, (c) Sub-System C of the open loop response in Figure 4.7.

4.6 RESULTS AND ANALYSIS

4.7 Actuator geometrical parameters

The presented didactic geometry shown in table 1 of HDEA designed for this research was done by taking in consideration patterns in its dimensions that can optimize its force and deformation in the z-axis, such as the complementary angle α , which is designed to be very close to $\pi/2$ for this purpose. Furthermore, all the equations presented in this study are parametrized as general as possible; thus, this model should apply to any

HDEA geometry or dielectric elastomer material. Furthermore, the dimensions and dynamics of the electrodes between the elastomers are not taken into consideration in this study.

Table 4.1. *Initial elementary parameters of the HDEA.*

Parameter [units]	Description
$R_{o_0} = 0.030$ [m]	External radius
$R_{i_0} = 0.010$ [m]	Internal radius
$z_0 = 0.001$ [m]	Elastomer thickness
$N_p = 50$ [-]	Number of periods in the HDEA
$N_e = 2$ [-]	Number of elastomers in series.
$M_{HDEA} = 0.2413$ [Kg]	Mass of the Actuator

Material parameters

This study applied the material parameters of the didactic material VHB 4910 for its extensive coverage in literature. Numerous studies have verified that its hyperelasticity response matches Yeoh's non-linear hyperelastic strain energy model (Wissler & Mazza, 2005b). Furthermore, because it is difficult to find viscoelastic parameters for a specific

viscoelasticity model and a consistency of data in the literature, the lumped parameter model applied to the generalized Kelvin-Mawells model is used in this educational method. First, the actuator dynamics were tested with no load attached but just its intrinsic weight and applying the maximum voltage admissible (right before electromechanical instability) for a VHB 4910 material without pre-stretch (Gbaguidi et al., 2016). Further, the parameters for the generalized Kelvin-Mawells viscoelastic model were tuned in order to get a viscous response similar to those presented in the literature (Wissler & Mazza, 2007c). In addition, once desirable parameters were obtained, the voltage was reduced to zero in order to see if the actuator stayed completely undeformed in order to check that the intensity of the parameters could effect a back contraction on the actuator, meaning that they were too large values or any other undesired effect. Notice, it is important to mention that the parameters obtained to represent the viscoelastic response were tuned and designed from the specification of the author and may not represent the real parameter for viscoelasticity of VHB 4910.

Table 4.2. *Hyperelastic and viscoelastic material parameters.*

Parameter [units]	Description
$C_{10} = 0.0693$ [MPa]	Yeoh's model parameter.
$C_{20} = -8.88 * 10^{-4}$ [MPa]	Yeoh's model parameter.
$C_{30} = 16.7 * 10^{-6}$ [MPa]	Yeoh's model parameter.
$N_V = 1875 * 10^{-6}$ [MPa.s]	Viscosity of the dashpot N_V
$K_1 = 0.106116$ [MPa]	Elastic constant of spring K1
$N_1 = 0.033966$ [MPa.s]	Viscosity of the dashpot N1
$K_2 = 0.045510$ [MPa]	Elastic constant of spring K2
$N_2 = 0.103008$ [MPa.s]	Viscosity of the dashpot N2
$K_3 = 0.016139$ [MPa]	Elastic constant of spring K3
$N_3 = 7.108662$ [MPa.s]	Viscosity of the dashpot N3
$K_4 = 0.010922$ [MPa]	Elastic constant of spring K4
$N_4 = 47.91$ [MPa.s]	Viscosity of the dashpot N4

4.8 Actuator dynamic responses

The response of the actuator was tested under different circumstances. First, as shown in

Figure 4.9, the actuator was feed with a step input voltage and holding a weight of 10 N. The response of the states can be found in Figure 4.9 and Figure 4.10. Furthermore, it can be notice that it took less than 250 milliseconds to the actuator to star reaching a steady state value. In addition, it can be appreciated, that the external radius (Figure 4.10 (a)) increases as the actuator is contracted (Figure 4.9 top) and it decreased as the actuator is lengthened. Second, as shown in Figure 4.11. The length of the actuator was studied by applying a sinusoidal voltage with the same load condition of 10 N of an attached mass.

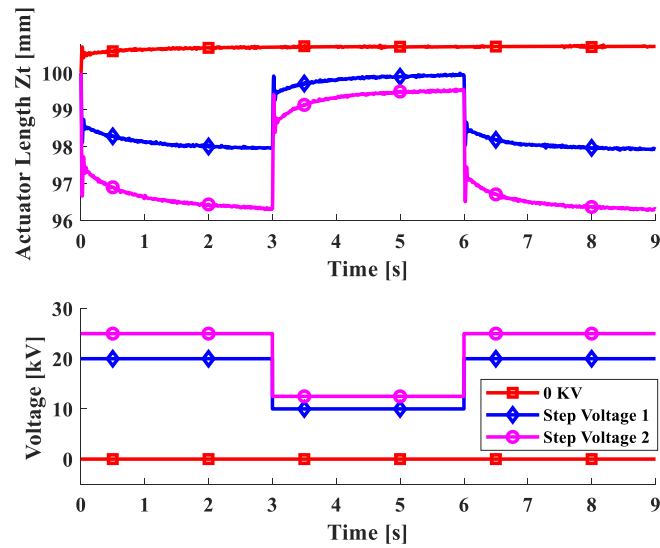


Figure 4.9. Trainsient response of a step input voltage. On top actuator length vs. time, bottom voltage applied vs. time.

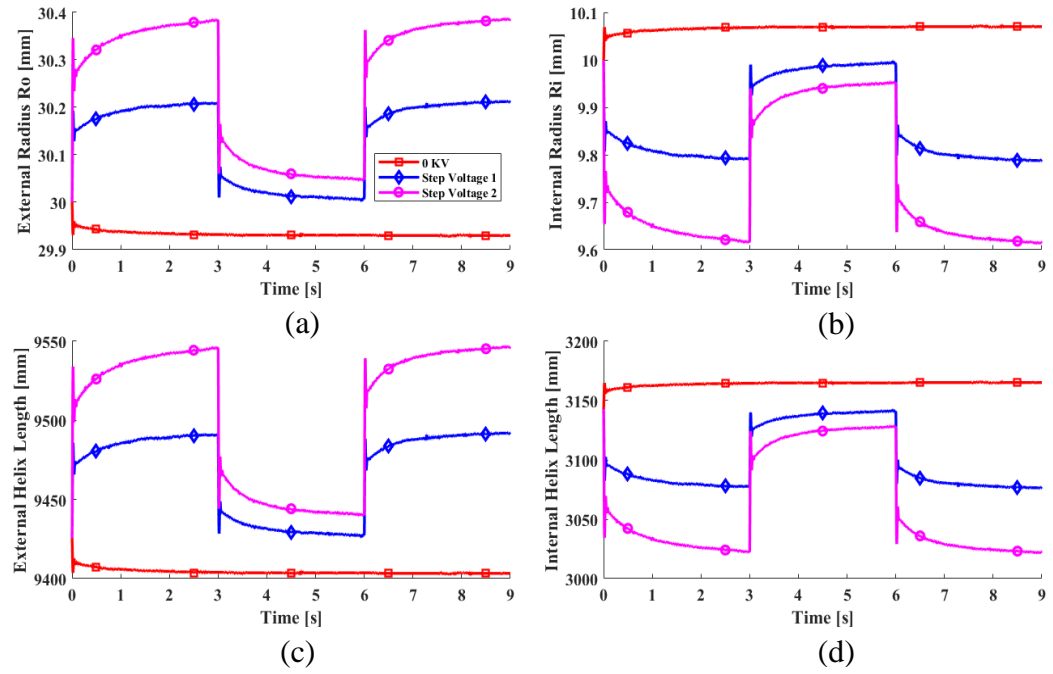


Figure 4.10. Transient response of a step input voltage.

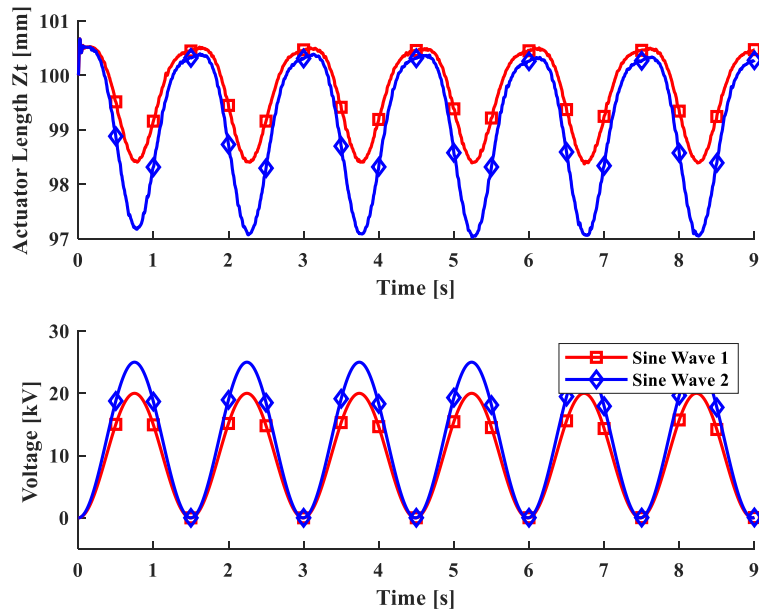


Figure 4.11. Transient response of an input voltage with form of a sinusoidal wave.

As a further means to evaluate the performance of the actuator, the open loop response of the stroke of the actuator was studied without any electrostatic force for 9 seconds as shown in *Figure 4.12*. To continue, a constant increase in voltage of 5.5 Volts was applied every 1 millisecond interval until it reached 25KV which is theoretical possible since it is a value earlier the electromechanical instability of the material under Yeoh's model (Gbaguidi et al., 2016), and then in reverse with a total duration of 9 seconds. This frequency of input voltage was repeated three times with different amounts of load attached to the actuator as shown in *Figure 4.13*. It can be appreciated how a small hysteresis appears on the actuator under these conditions, because the ratio on the elongations is small (*Figure 4.13*). Furthermore, it can be realized that the actuator is contracting around 3.5% of its length when lifting 30 N which 12.5 times its own weight; however, these results could be improved with more accurate parameters for the model.

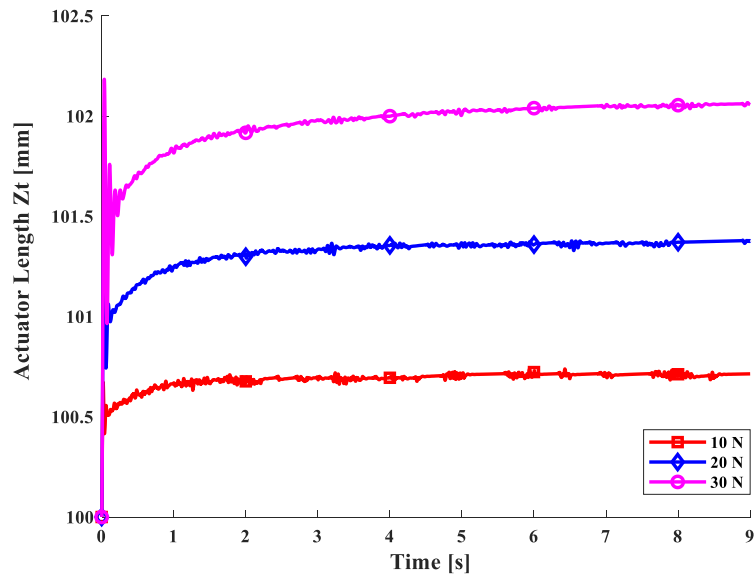


Figure 4.12. Deformation of the actuator length under different loads without the

presence of the electrostatic pressure.

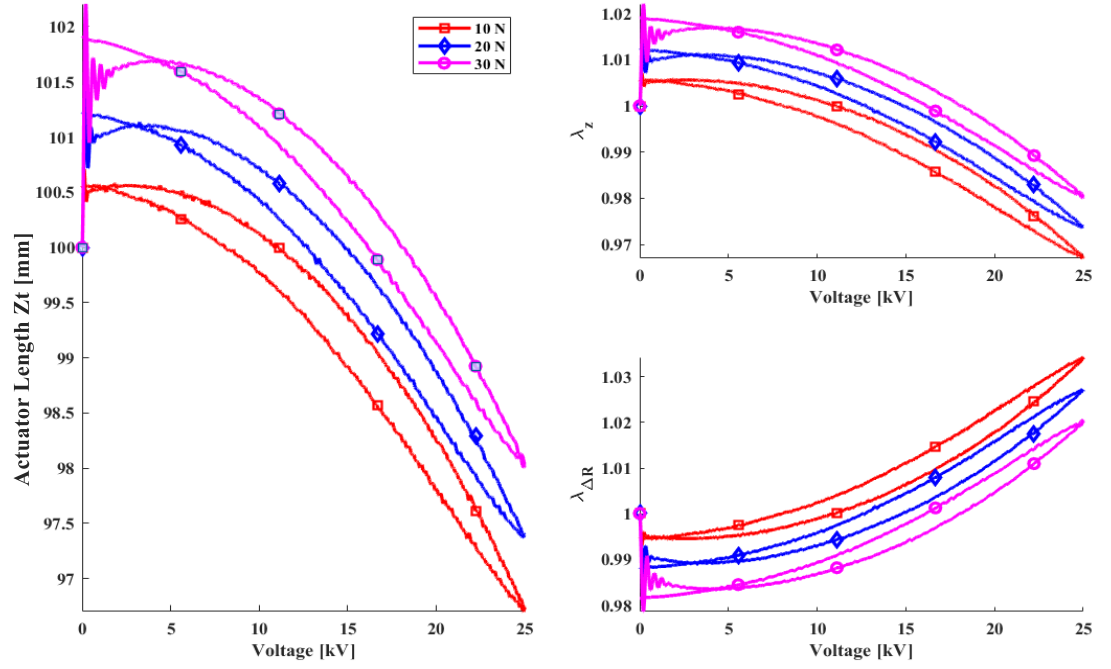


Figure 4.13. Deformation of the actuator length and principal stretches while holding different loads under electrostatic pressure.

Furthermore, the complementary angle $\alpha(t)$ was also studied. Figure 4.14 highlights that the variation of the complementary angle is insignificant and very close to $\pi/2$, which means that around 99% of the electrostatic force is directed to the z-axis for the HDEA geometry presented in this research as shown in Table 4.1.

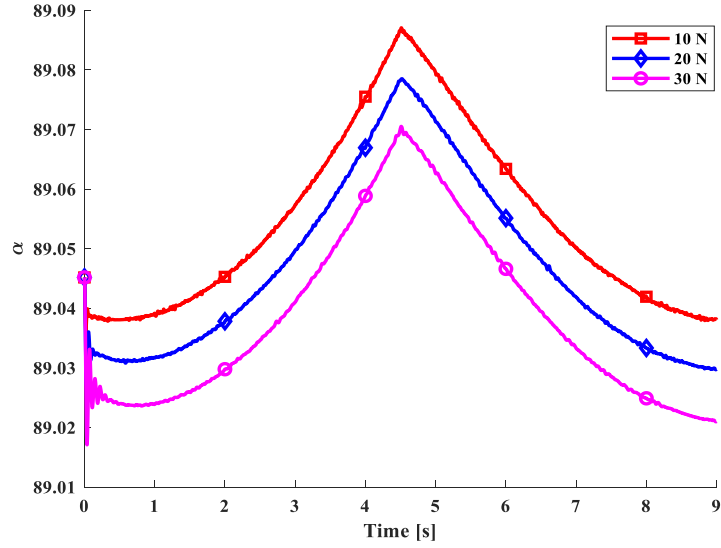


Figure 4.14. Complementary angle $\alpha(t)$ vs. time when the HDEA is under the conditions shown in *Figure 4.13*.

Finally, the electrical current and power consumption of the actuator was considered. Figure 4.15 shows the electrical performance of the actuator, where the current drawn comes from the compliant capacitor and the varying resistance that forms part of the morphology of the actuator. Furthermore, it can be appreciate in Figure 4.15 that the three cases shown in Figure 4.15 consume the same amount of power because more power will be needed to compress the actuator for the 20 N and 30 N external load cases as much as the 10 N case. Lastly, the electrical properties of the material used in this research can be gleaned from table 3.

Table 4.3. *Electrical properties of the elastomer used.*

Parameter [units]	Description
$\epsilon_r = 4.7$ [-]	Dielectric permittivity.
$\rho = 3.1 * 10^8$ [$\Omega . m$]	Electrical resistivity.

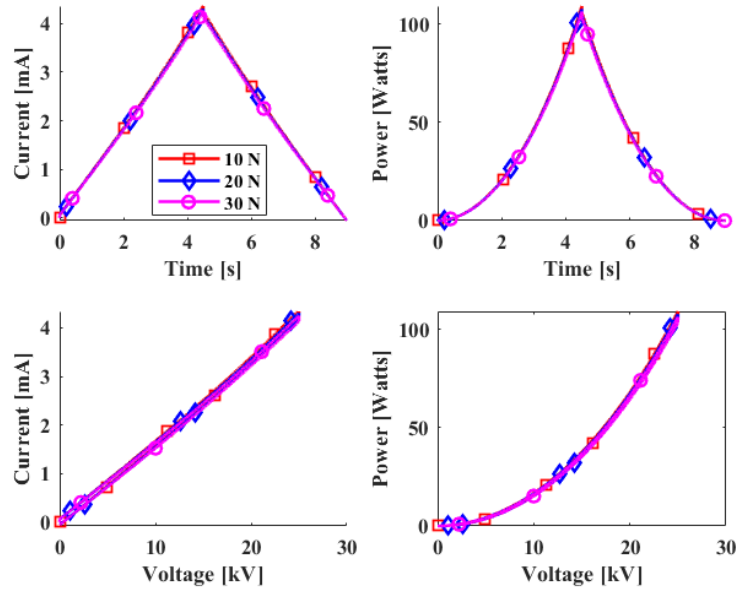


Figure 4.15. Current and power consumption vs voltage and time when the HDEA is under the conditions shown in Figure 4.13.

4.9 CONCLUSION AND FUTURE WORK

Dielectric elastomer actuators are devices in which their dynamics not only depend on the geometrical morphology of the actuator, but also most notably on the intrinsic

characteristics of the material used. As shown in previous equations, tables, and plots, the actuator depends on many different material parameters such as the dielectric permittivity in addition to those defining hyperelasticity and viscosity models, which can be found by doing many different mechanical and electrical tests. Some experiments are simple to perform, such as the measurement of the dielectric permittivity. However, in the mechanical domain and more precisely if working with hyperelasticity, the parameters need to be fitted from different modes of deformation at the same time, such as uniaxial, biaxial, and so forth. Even relaxation tests are also needed in order to obtain parameters that govern that viscous behavior. Consequently, from an applications point of view, it is needed and will be part of the future work of the authors, to design a non-linear parameter estimator to get these parameters by doing an inverse problem; this parameter estimator bypasses the need to perform experiments where the parameters are calculated by complex means. Furthermore, a HDEA will be fabricated from which data will be extracted as the input for the estimator in future. Finally, a numerical simulation and experimentation on HDEA prototype will be performed to validate the presented dynamics on this research.

Chapter 5 Enhancing the Dielectric Constant of Dielectric Elastomer Actuators

5.1 Introduction

Dielectric elastomer actuators are among best candidates for creating efficient artificial muscles. However, they suffer from the need of application of high voltages in the order of kilo volts to get some decent deformation. Meanwhile it can be notice from Equation (2.1) that the dielectric permittivity ϵ_r is an electrical material parameter that is proportional to the electrostatic pressure that compress the material; thus, it can be intuitively predicted that an increase of this parameter could provide a higher amount of pressure while maintaining the same amount of voltage. Therefore, many techniques to increment the dielectric constant of elastomeric materials are currently under research. In this research, polymer matrices are mixed with ceramic fillers of a high dielectric constant to create new composites that have an increase of their dielectric permittivity when compare with their basic form.

5.2 Composite formulation

To design the composites, different elastomers were taking in consideration. The main idea is to choose an elastomer with a long elongation modulus and softness, because it is easier for soft elastomers to be compressed by the electrostatic pressure. Then the polymer matrix is mixed with a filler that have a higher dielectric constant, the resulting composite have an elevated dielectric constant (Figure 5.1). Furthermore, it is tangibly that by adding solid fillers in the mixture causes a decrease in the softness of the

elastomeric material. Thus, it can be assumed that the Young's modulus of the overall composite will increase. Therefore, it is important that an increase on the dielectric permittivity does not compromises the softness of the material.

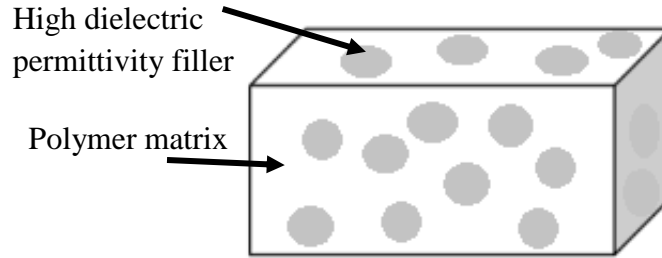


Figure 5.1. Generic polymer matrix mixed with fillers of high dielectric constant.

Table 5.1 provides information about the elastomeric materials used for this study. Dow Corning Sylgard 184 was selected, because it is a soft elastomer that can be cured by the application of heat; thus, reducing curing time from several hours to minutes which makes it an attractive material to be used for 3D printing in future research.

The other elastomer under study was the BJB TC-5005 A/B-C. This elastomeric material is comprised of three parts. Part A is the elastomer and Part B is the catalyst, which start the curing reaction, then part C is added with the intention of making the elastomer softer. The more part C is added the softer the material will be. However, more than 50% of the total mix cannot be part C or the polymer will be unstable.

Table 5.1. *Elastomeric materials to be used as a polymer matrix.*

Material	Dielectric Constant @ 100Hz	Dielectric Constant @ 100kHz	Elongation at break [%]	Cure Time @ 25°C [hr]
Dow Corning Sylgard 184	2.72	2.68	140	48
BJB TC-5005	5.2	4.2 (1 MHz)	700	>24

The fillers are chosen for the creation of the new composites are Calcium Cooper Titanate (CCTO) and Barium Titanate (BaTiO₃) because of their extraordinary dielectric permittivity. Notice that theses fillers comes in the form of Nano powders as shown in

Error! Reference source not found.. *Ceramic fillers with high dielectric constant.*

Filler	Dielectric Constant[8]	Particle size
Calcium Copper Titanate (100-300 nm)	> 9000-12000	1.8 um
Barium Titanate (50 nm)	~6000	400 nm

5.3 Experiment

The elastomers and filler were mixed using a planetary mixer THINKY ARE-310 (Figure

5.3) in which the were mixed at 2000 rpms and later poured into molds. The composites stay in the mold for 24 hours at room temperature to get cure, then they were cut into square samples (Figure 5.2).

BJB TC 5005 out of the mold after 24h curing

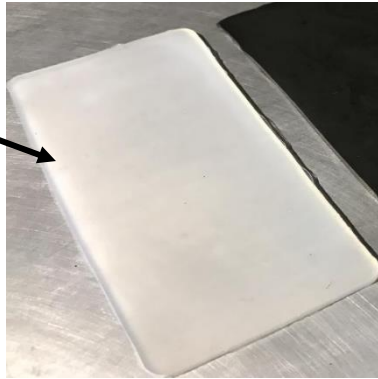


Figure 5.2. Coupon of plain BJB TC-5005.



Figure 5.3. THINKY MIXER ARE-310.

In order to calculate the relative permittivity of the composites, the formula of a parallel

plate capacitor is used (5.1). Therefore, the capacitance of the coupons have to be measure experimentally and then solved for the dielectric constant using Equation (5.1). To measure the capacitance it is necessary to attach two conductive plates in both sides of each sample, in this case, aluminum plates where used. To continue, an LCR Meter (Figure 5.4) is connected to each plate, and then the capacitance is measured respectively. The measurement is performed at different frequencies to study the changes that it generate to the dielectric constant. The following expression relates the capacitance of the coupons with the permittivity of interest.

$$C = \frac{\epsilon A}{d} \quad (5.1)$$

Where A represents the area of the aluminum plates, which is calculated to be $1.439 \times 10^{-3} m^2$; ϵ is defined as the absolute permittivity of the material and d is the thickness of the samples being tested, which in this case are approximately 0.0022 m. Once the absolute permittivity is obtained from Equation (5.1), the relative permittivity is calculated using the following expression. Where ϵ_o is defined as the vacuum permittivity, with a value of $8.854 \times 10^{-12} F/m$. Furthermore, it is recommended that the parallel plates need to be a bit smaller than the coupons; thus, undesired electrical effects occurs and damage the reading. In Figure 5.4, it is possible to appreciate the main setup to determine capacitance.

$$\epsilon = \epsilon_r \epsilon_o \quad (5.2)$$

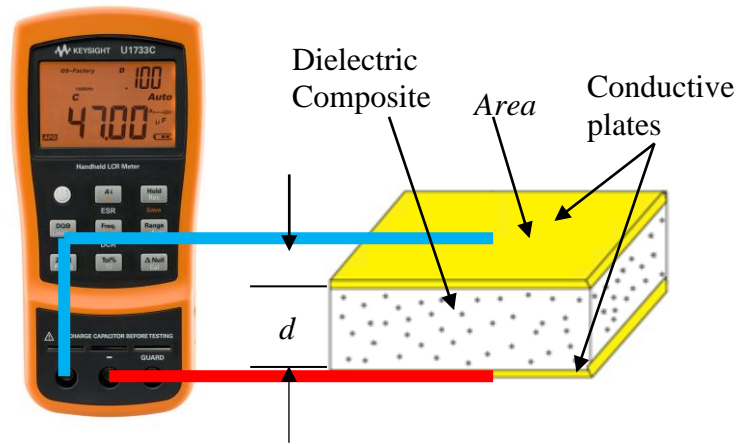


Figure 5.4. LCR meter and composite for capacitance measurement.

5.4 Results

The first study was performed on the BJB TC-5005 elastomer in combination with BaTiO₃. The elastomer composite was created with 45% of part C to make it as soft as possible without reaching the limit where it become unstable (50%). The results in Figure 5.5 show an increase of the dielectric permittivity up to 400% for the case 37.5% of the mixture was BaTiO₃ and a 200% when just 10% of filler was added to the mixture. Furthermore, it shows that if the frequency is increased, the dielectric permittivity decreases, which is phenomenon described in the literature (Brochu & Pei, 2010). The accuracy of the method used to measure the dielectric permittivity can be proved because the results obtained by the BJB without any fillers match the dielectric permittivity documented from the manufacturer.

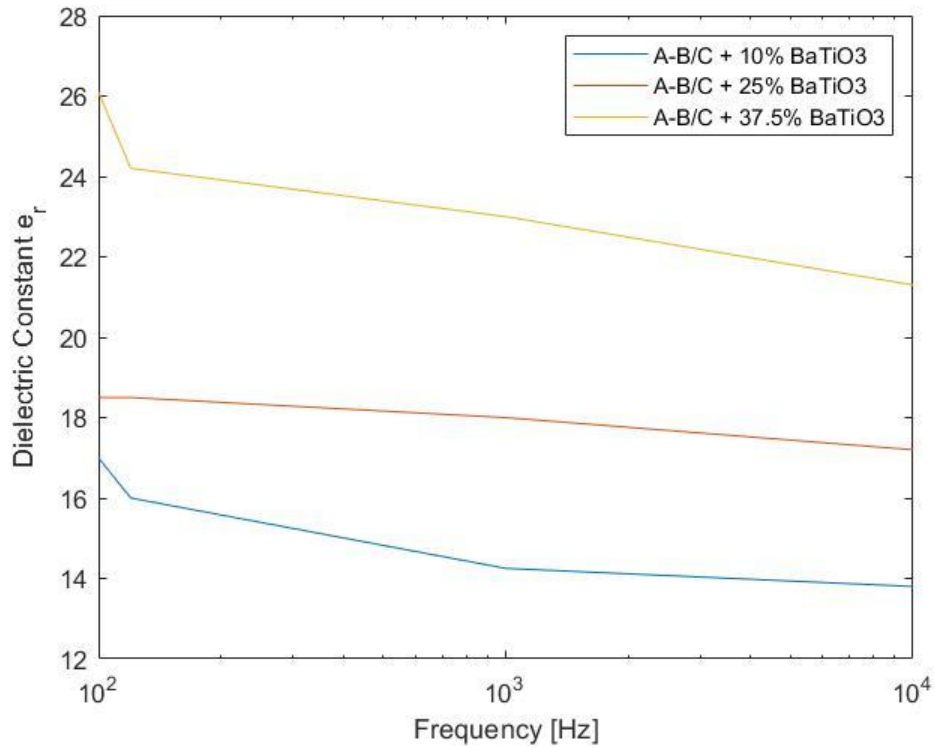


Figure 5.5. BJB TC-5005 (45% of C) combined with BaTiO₃ add different volume fractions.

Furthermore, the study continues with the creation of composites where Sylgard 184 is the polymer matrix, and BaTiO₃ and CCTO are the fillers. In this case, Figure 5.6 and Figure 5.7 provide with information that the dielectric constant is monotonically increasing as the concentration or weight fraction from the fillers is increased in the mixture. It is notorious in this case that although CCTO has a base dielectric constant much high than BaTiO₃ the overall dielectric constant of both composites is increased almost the same. Meaning that the chemical composition of the polymer matrix is also important to properly couple with the filler.

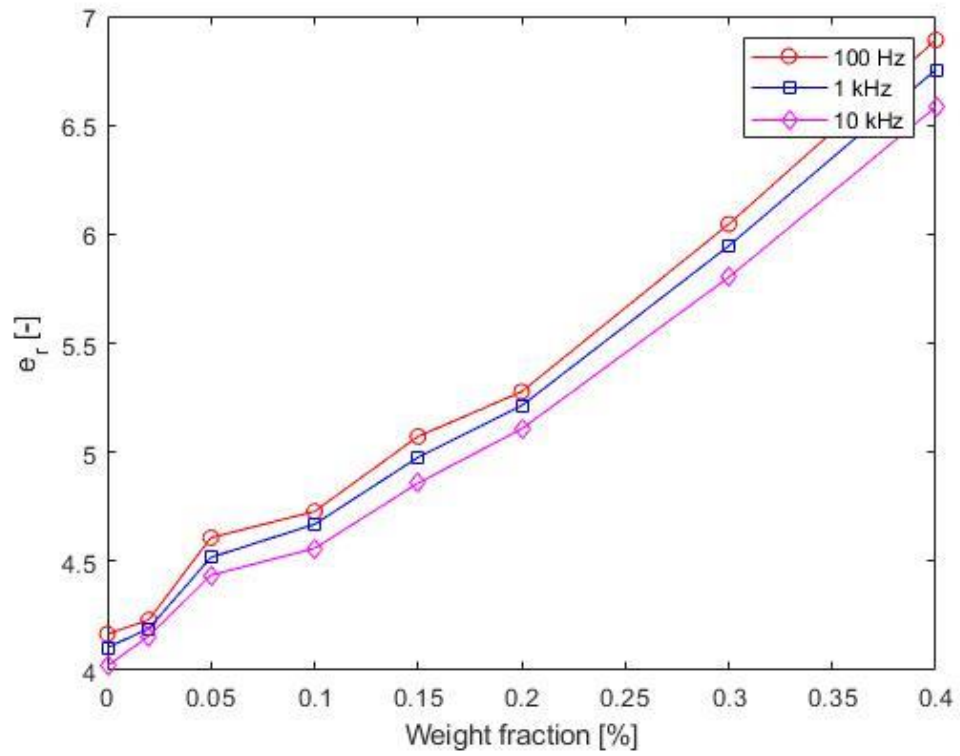


Figure 5.6. Measure of dielectric constant of Sylgard 184 composite that is mixed in a (15:1) ratio with the addition of BaTiO₃ fillers at different weight fractions, and tested at different frequencies.

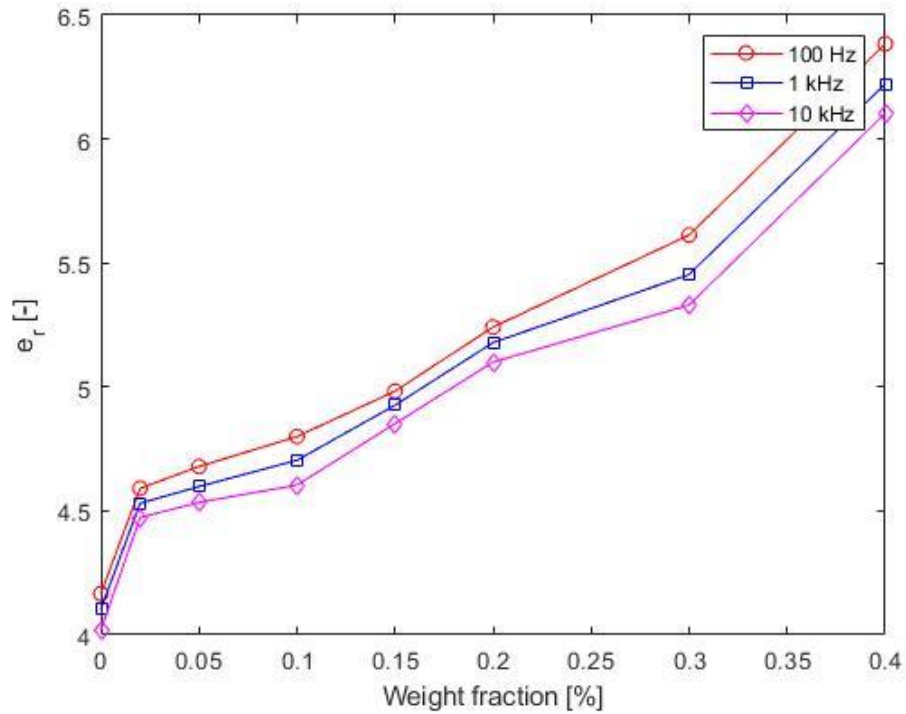


Figure 5.7. Measure of dielectric constant of Sylgard 184 composite that is mixed in a (15:1) ratio with the addition of CCTO fillers at different weight fractions, and tested at different frequencies.

5.5 Conclusions

The application of ceramic fillers increases the dielectric constant of DEAs. However, it also decreases the softness of the materials which means there is an increase in the modulus of elasticity and therefore less hard to deform.

Although CCTO is the ceramic filler with the highest dielectric constant it does not provide a high increase in the dielectric constant of the overall composite. However, other elastomers need to be investigated to look for a better outcome.

One of the drawbacks from BJB TC 5005 A/B-C is that it is not cured by heat but by condensation. Therefore, although it is a soft material and fillers tend to increase its dielectric constant, at this moment is not a material that can be used for 3D printing because it takes more than 24 h to cure which is not a good characteristic for rapid prototyping.

CONCLUSION

As show in chapter three, the methodology presented in this study can be utilized for the derivation of dynamic models for multilayer dielectric elastomer actuators. The study prove that error occurring between analytical and numerical model is small and is due to simplification between a one-dimensional problem against and three dimensional respectively. The inertial mass of the actuator also played an important role in the accuracy of the model, assuming that just half of the mass of the actuator is deformed provided with a simplification of the equations however it increases the error between analytical and numerical model. Furthermore, chapter 3 illustrate that the analytical model can be used to test control system. In this particular case, a PID controller was tested; however, it found troublesome to follow a path because of the nonlinearity of the system; furthermore, it can be intuitively predicted that the error will continue to build up as time passes because of the viscoelastic nature of the actuator. The controller also used feedback from the analytical model of the capacitance of the actuator rather than utilizing a direct measurement of deformation.

In chapter 4, a particular geometrical configuration of the multilayer DEA was presented, the HDEA. I was prove that by following the same methodology as chapter 3, it was able to derive the dynamics of the system. However, it also proved that as geometry gets complex, the system increases its nonlinearity, which can also be hypothesized that it will be same case if the number of degrees of freedom increases. Finally, it also proved that for helical actuators the complementary angle α can plays a major role on the simplification of the system. This is due because for values of α close to 90 degrees the

actuator start to behave like a regular cylindrical DEA which equation are simpler than HDEA.

Modeling of DEAs requires a large number of electrical and mechanical material parameters. As an example, material parameters that define strain energy functions for hyperelasticity such as Yeoh, Ogden or Mooney Rivlin require special equibiaxial equipment and nonlinear curve fitting. Furthermore, the obtaining of material parameter for viscoelasticity requires relaxation test on the material, which means that cyclic loading and curve fitting have to be applied over many coupons on the material under study. Therefore, if a physical device exists but not the necessary tools to obtain the parameter parameters for the analytical model, it is better to use an alternative method for finding dynamics such as system identification or machine learning techniques.

The elevated difficulty for the fabrication of DEA makes that most prototypes are made handcrafted, which, usually do not provide with accurate experimental data or repeatability. Therefore, utilizing analytical equations to model dynamics of DEA can be tempting to be used for optimization and to test control systems. However, as geometrical complexity increases, degrees of freedoms and the incorporation of other physics such as electrothermal deformation, analytical dynamical models tend to be over cumbersome and not an elegant solution.

FUTURE WORK

The methodology used in this work can be further expanded for deriving dynamical models of dielectric elastomers with multiple degrees of freedom. When the electrodes of a dielectric elastomer are sectioned, they can perform bending and torsion movements. Furthermore, long-term effects can also be added to the model, such as electrothermal stress, which causes deformation due to heat that comes from the application of high voltage. There are studies that derive electrothermal stress in DEAs but these studies mostly in steady state cases (Christensen et al., 2018); thus, the transient accumulation of heat is not taken in consideration. Furthermore, as the actuator lifetime increases, ageing effect occurs on the elastomer making it softer and thus changing the relationship between input and output (Bele et al., 2016).

Utilizing dynamic equations can become very complex when the complexity of the actuator increases; therefore, utilizing machine learning techniques such as deep reinforcement learning could become useful for learning complex and time dependent models when a physical version of the actuator is available. One tentative option is the use of deep reinforcement learning which utilizes a combination of Markov decision process and neural networks (Mnih et al., 2015) to learn dynamical systems when no previous knowledge its behavior is known.

Among smart materials, DEAs are one of the most promising for the application in biotechnology. Utilization of DEAs for powered prosthetic such as exoskeletons and artificial limbs could be a game change in the quality and functionality of these devices. Meanwhile, controlling DEAs is a complicated challenge because of the nonlinearity of

the system; this fact in combination with the difficult task of providing an acceptable human machine interaction is an interesting topic of research. The utilization of artificial intelligence as a control method for DEAs while receiving input signals such as electromyography (EMG) from human (Carpi et al., 2009) could generate a good impact in field of biomedical devices for rehabilitation and human enhancement.

References

- 3M Inc. (2018). *3MTM VHBTM tape - specialty tape 4905*.
- Advani, S., Hosman, R., Lawrence, B., & Schuring, J. (2003). A full-flight simulator of the 1903 Wright Flyer. *AIAA Modeling and Simulation Technologies Conference and Exhibit*. <https://doi.org/10.2514/6.2003-5815>
- Al-Fahaam, H., Davis, S., & Nefti-Meziani, S. (2018). The design and mathematical modelling of novel extensor bending pneumatic artificial muscles (EBPAMs) for soft exoskeletons. *Robotics and Autonomous Systems*, 99, 63–74.
<https://doi.org/10.1016/j.robot.2017.10.010>
- Ali, A., Hosseini, M., & Sahari, B. B. (2010). *A Review of Constitutive Models for Rubber-Like Materials*. 3(1), 232–239.
- Alibakhshi, A., & Heidari, H. (2020). Nonlinear dynamics of dielectric elastomer balloons based on the Gent-Gent hyperelastic model. *European Journal of Mechanics, A/Solids*, 82(October 2019), 103986.
<https://doi.org/10.1016/j.euromechsol.2020.103986>
- Ang, B. W. K., & Yeow, C. H. (2019). Design and characterization of a 3d printed soft robotic wrist sleeve with 2 DoF for stroke rehabilitation. *RoboSoft 2019 - 2019 IEEE International Conference on Soft Robotics*, 577–582.
<https://doi.org/10.1109/ROBOSOFT.2019.8722771>

- Barnes, A., Liu, Q., Young, G., & Lu, T. F. (2007). Evaluation of selected dielectric elastomers for use in an artificial muscle actuator. *Proceedings of the Australasian Conference on Robotics and Automaton*.
<http://www.araa.asn.au/acra/acra2007/papers/paper12final.pdf>
- Berlinger, F., Duduta, M., Gloria, H., Clarke, D., Nagpal, R., & Wood, R. (2018). A Modular Dielectric Elastomer Actuator to Drive Miniature Autonomous Underwater Vehicles. *Proceedings - IEEE International Conference on Robotics and Automation*, c, 3429–3435. <https://doi.org/10.1109/ICRA.2018.8461217>
- Bindu.Sl*, H.A Mangalvedekar1, S. U., & Archana Sharma2, D. P. Chakravarti2, P.C Saro/, K. C. M. (2012). *Experimental Study on Permittivity of Acrylic Dielectric Elastomer*. 2(I), 1–4.
- Branz, F., & Francesconi, A. (2017). Experimental evaluation of a Dielectric Elastomer robotic arm for space applications. *Acta Astronautica*, 133, 324–333.
<https://doi.org/10.1016/j.actaastro.2016.11.007>
- Brochu, P., & Pei, Q. (2010). Advances in Dielectric Elastomers for Actuators and Artificial Muscles. *Macromolecular Rapid Communications*, 31(1), 10–36.
<https://doi.org/10.1002/marc.200900425>
- Cao, C., Burgess, S., & Conn, A. T. (2019). Toward a dielectric elastomer resonator driven flapping wing micro air vehicle. *Frontiers Robotics AI*, 6(JAN).
<https://doi.org/10.3389/frobt.2018.00137>

- Cao, C., Gao, X., Burgess, S., & Conn, A. T. (2020). Power optimization of a conical dielectric elastomer actuator for resonant robotic systems. *Extreme Mechanics Letters*, 35(xxxx), 100619. <https://doi.org/10.1016/j.eml.2019.100619>
- Cao, W., Cudney, H. H., & Waser, R. (1999). Smart materials and structures. *Proceedings of the National Academy of Sciences of the United States of America*, 96(15), 8330–8331. <https://doi.org/10.1073/pnas.96.15.8330>
- Carpi, F., & de Rossi, D. (2012). Small-strain modeling of helical dielectric elastomer actuators. *IEEE/ASME Transactions on Mechatronics*, 17(2), 318–325. <https://doi.org/10.1109/TMECH.2010.2100403>
- Carpi, F., Migliore, A., Serra, G., & Rossi, D. De. (2005). Helical dielectric elastomer actuators. *Smart Materials and Structures*, 14(6), 1210–1216. <https://doi.org/10.1088/0964-1726/14/6/014>
- Carpi, F., Salaris, C., & de Rossi, D. (2007). Folded dielectric elastomer actuators. *Smart Materials and Structures*, 16(2). <https://doi.org/10.1088/0964-1726/16/2/S15>
- Carpi, F., Salaris, C., & De Rossi, D. (2007). Folded dielectric elastomer actuators. *Smart Materials and Structures*, 16(2). <https://doi.org/10.1088/0964-1726/16/2/S15>
- Caspari, P., Dünki, S. J., Nüesch, F. A., & Opris, D. M. (2018). Dielectric elastomer actuators with increased dielectric permittivity and low leakage current capable of suppressing electromechanical instability. *Journal of Materials Chemistry C*, 6(8), 2043–2053. <https://doi.org/10.1039/c7tc05562e>

- Conn, A. T., & Rossiter, J. (2012). Towards holonomic electro-elastomer actuators with six degrees of freedom. *Smart Materials and Structures*, 21(3).
<https://doi.org/10.1088/0964-1726/21/3/035012>
- Della Schiava, N., Thetpraphi, K., Le, M. Q., Lermusiaux, P., Millon, A., Capsal, J. F., & Cottinet, P. J. (2018). Enhanced figures of merit for a high-performing actuator in electrostrictive materials. *Polymers*, 10(3), 1–15.
<https://doi.org/10.3390/polym10030263>
- Duduta, M., Hajiesmaili, E., Zhao, H., Wood, R. J., & Clarke, D. R. (2019). Realizing the potential of dielectric elastomer artificial muscles. *Proceedings of the National Academy of Sciences of the United States of America*, 116(7), 2476–2481.
<https://doi.org/10.1073/pnas.1815053116>
- Dynamics, S., & Forum, G. S. (2001). *Paper # 2001-1492 Electroactive Polymers as Artificial Muscles – Reality and Challenges Yoseph Bar-Cohen NDEAA Technologies , JPL / Caltech , Pasadena , CA.*
- Fancello, E., Ponthot, J. P., & Stainier, L. (2006a). A variational formulation of constitutive models and updates in non-linear finite viscoelasticity. *International Journal for Numerical Methods in Engineering*, 65(11), 1831–1864.
<https://doi.org/10.1002/nme.1525>
- Fancello, E., Ponthot, J. P., & Stainier, L. (2006b). A variational formulation of constitutive models and updates in non-linear finite viscoelasticity. *International*

Journal for Numerical Methods in Engineering, 65(11), 1831–1864.

<https://doi.org/10.1002/nme.1525>

García Ruíz, J., & Yarime Suárez, L. (2006). Comparison of hyperelastic material models in the analysis of fabrics. *International Journal of Clothing Science and Technology*, 18(5). <https://doi.org/10.1108/09556220610685249>

Gbaguidi, A., Konduru, V. K., & Kim, D. (2016). *Analytical approach on the performance of helical dielectric elastomer actuator*. 9798, 979814. <https://doi.org/10.1117/12.2219911>

Goriely, A., Destrade, M., & Amar, M. B. E. N. (2006). Instabilities in elastomers and in soft tissues. *The Quarterly Journal of Mechanics & Applied Mathematics*. <https://doi.org/10.1093/qjmam/hbl017>

Gu, G. Y., Zhu, J., Zhu, L. M., & Zhu, X. (2017a). A survey on dielectric elastomer actuators for soft robots. *Bioinspiration and Biomimetics*, 12(1). <https://doi.org/10.1088/1748-3190/12/1/011003>

Gu, G. Y., Zhu, J., Zhu, L. M., & Zhu, X. (2017b). A survey on dielectric elastomer actuators for soft robots. *Bioinspiration and Biomimetics*, 12(1). <https://doi.org/10.1088/1748-3190/12/1/011003>

Hackl, C., Hong-Yue Tang, Lorenz, R. D., Turng, L., & Schroder, D. (2005). A multidomain model of planar electro-active polymer actuators. *Conference Record of the 2004 IEEE Industry Applications Conference, 2004. 39th IAS Annual*

- Meeting.*, 3(5), 2125–2130. <https://doi.org/10.1109/IAS.2004.1348760>
- He, T., Cui, L., & Chen, C. (2009). Large deformation analysis of a dielectric elastomer membrane-spring system. *Second International Conference on Smart Materials and Nanotechnology in Engineering*, 7493, 74935H. <https://doi.org/10.1117/12.840905>
- Hise, P. (2003, March 1). *The 1903 Wright Flyer*. Air & Space Magazine.
<https://www.airspacemag.com/how-things-work/the-1903-wright-flyer-3867542/>
- Hodgins, M., Rizzello, G., Naso, D., York, A., & Seelecke, S. (2014). An electro-mechanically coupled model for the dynamic behavior of a dielectric electro-active polymer actuator. *Smart Materials and Structures*, 23(10).
<https://doi.org/10.1088/0964-1726/23/10/104006>
- Hoffstadt, T., & Maas, J. (2015a). Analytical modeling and optimization of DEAP-based multilayer stack-transducers. *Smart Materials and Structures*, 24(9), 94001.
<https://doi.org/10.1088/0964-1726/24/9/094001>
- Hoffstadt, T., & Maas, J. (2015b). Analytical modeling and optimization of DEAP-based multilayer stack-transducers. *Smart Materials and Structures*, 24(9), 94001.
<https://doi.org/10.1088/0964-1726/24/9/094001>
- Hu, P., Huang, Q., Madsen, J., & Ladegaard Skov, A. (2020). *Soft silicone elastomers with no chemical cross-linking and unprecedented softness and stability*. 1137517(April 2020), 33. <https://doi.org/10.1117/12.2557003>

- Jean-Mistral, C., Sylvestre, A., Basrour, S., & Chaillout, J. J. (2010a). Dielectric properties of polyacrylate thick films used in sensors and actuators. *Smart Materials and Structures*, 19(7). <https://doi.org/10.1088/0964-1726/19/7/075019>
- Jean-Mistral, C., Sylvestre, A., Basrour, S., & Chaillout, J. J. (2010b). Dielectric properties of polyacrylate thick films used in sensors and actuators. *Smart Materials and Structures*, 19(7). <https://doi.org/10.1088/0964-1726/19/7/075019>
- Joudzadeh, P., Hadi, A., Tarvirdizadeh, B., Borooghani, D., & Alipour, K. (2019). Design and fabrication of a lower limb exoskeleton to assist in stair ascending. *Industrial Robot: The International Journal of Robotics Research and Application*, 46(2), 290–299. <https://doi.org/10.1108/ir-09-2018-0199>
- Jung, H. S., Yang, S. Y., Cho, K. H., Song, M. G., Nguyen, C. T., Phung, H., Kim, U., Moon, H., Koo, J. C., Nam, J. do, & Choi, H. R. (2017). Design and fabrication of twisted monolithic dielectric elastomer actuator. *International Journal of Control, Automation and Systems*, 15(1). <https://doi.org/10.1007/s12555-016-0466-z>
- Katzschmann, R. K., DelPreto, J., MacCurdy, R., & Rus, D. (2018). Exploration of underwater life with an acoustically controlled soft robotic fish. *Science Robotics*, 3(16), 1–13. <https://doi.org/10.1126/SCIROBOTICS.AAR3449>
- Khajehsaeid, H., Arghavani, J., & Naghdabadi, R. (2013). A hyperelastic constitutive model for rubber-like materials. *European Journal of Mechanics, A/Solids*, 38, 144–151. <https://doi.org/10.1016/j.euromechsol.2012.09.010>

- Kim, D., El Atrache, A., Divo, E., & Drakunov, S. (2019). *A dynamic model of helical dielectric elastomer actuator*. *March*, 21. <https://doi.org/10.1117/12.2514382>
- Kim, D., Park, J. H., Divo, E., & El Atrache, A. (2018). *Optimization of helical dielectric elastomer actuator with additive manufacturing*. 32. <https://doi.org/10.1117/12.2296720>
- Kim, D., Park, J. H., Sikulskyi, S., Divo, E., & Martinez, R. (2019). *Numerical studies on origami dielectric elastomer actuator using Kresling pattern*. *March 2019*, 17. <https://doi.org/10.1117/12.2514374>
- Kim, J., Bae, S.-H., Kotal, M., Stalbaum, T., Kim, K. J., & Oh, I.-K. (2017). Polymer Actuators: Soft but Powerful Artificial Muscles Based on 3D Graphene-CNT-Ni Heteronanostructures (Small 31/2017). *Small*, 13(31). <https://doi.org/10.1002/sml.201770167>
- Kim, S., Laschi, C., & Trimmer, B. (2013). Soft robotics: A bioinspired evolution in robotics. *Trends in Biotechnology*, 31(5), 287–294. <https://doi.org/10.1016/j.tibtech.2013.03.002>
- Kofod, G., Sommer-Larsen, P., Kornbluh, R., & Pelrine, R. (2003). Actuation Response of Polyacrylate Dielectric Elastomers. *Journal of Intelligent Material Systems and Structures*, 14(12), 787–793. <https://doi.org/10.1177/104538903039260>
- Kolstad, J. L., & Tagg, F. L. (1984). *Pneumatic suspension system* (Patent No. US4580806A). United States Patent and Trademark Office.

- Kovacs, G., Düring, L., Michel, S., & Terrasi, G. (2009). Stacked dielectric elastomer actuator for tensile force transmission. *Sensors and Actuators, A: Physical*, 155(2), 299–307. <https://doi.org/10.1016/j.sna.2009.08.027>
- Kurimoto, M., Naya, K., Kato, T., & Suzuoki, Y. (2018). Influence of Elastomer Material and Stretch Direction on Relative Permittivity of Stretched Dielectric Elastomer. *2018 IEEE 2nd International Conference on Dielectrics, ICD 2018*, 83DUMMY. <https://doi.org/10.1109/ICD.2018.8468398>
- Lai, H. L., & Tan, C. A. (2016). Modeling the constraint effects of compliant electrodes in dielectric elastomers under uniaxial loading. *Proceedings of the Institution of Mechanical Engineers, Part C: Journal of Mechanical Engineering Science*, 230(15), 2623–2636. <https://doi.org/10.1177/0954406215602035>
- Laschi, C., & Cianchetti, M. (2014). Soft Robotics: New Perspectives for Robot Bodyware and Control. *Frontiers in Bioengineering and Biotechnology*, 2(January), 1–5. <https://doi.org/10.3389/fbioe.2014.00003>
- Lee, C., Kim, M., Kim, Y. J., Hong, N., Ryu, S., Kim, H. J., & Kim, S. (2017). Soft robot review. In *International Journal of Control, Automation and Systems* (Vol. 15, Issue 1). <https://doi.org/10.1007/s12555-016-0462-3>
- Llewellyn-Evans, H., Griffiths, C. A., & Fahmy, A. A. (2020). Design process and simulation testing of a shape memory alloy actuated robotic microgripper. *Microsystem Technologies*, 26(3). <https://doi.org/10.1007/s00542-019-04599-6>

- Madsen, F. B., Daugaard, A. E., Hvilsted, S., & Skov, A. L. (2016a). The Current State of Silicone-Based Dielectric Elastomer Transducers. *Macromolecular Rapid Communications*, 37(5), 378–413. <https://doi.org/10.1002/marc.201500576>
- Madsen, F. B., Daugaard, A. E., Hvilsted, S., & Skov, A. L. (2016b). The Current State of Silicone-Based Dielectric Elastomer Transducers. *Macromolecular Rapid Communications*, 37(5), 378–413. <https://doi.org/10.1002/marc.201500576>
- Madsen, F. B., Yu, L., Daugaard, A. E., Hvilsted, S., & Skov, A. L. (2014). Silicone elastomers with high dielectric permittivity and high dielectric breakdown strength based on dipolar copolymers. *Polymer*, 55(24), 6212–6219. <https://doi.org/10.1016/j.polymer.2014.09.056>
- Mirfakhrai, T., Madden, J. D. W., & Baughman, R. H. (2007). Polymer artificial muscles. *Materials Today*, 10(4), 30–38. [https://doi.org/10.1016/S1369-7021\(07\)70048-2](https://doi.org/10.1016/S1369-7021(07)70048-2)
- Mohammadi, A., Lavranos, J., Zhou, H., Mutlu, R., Alici, G., Tan, Y., Choong, P., & Oetomo, D. (2020). A practical 3D-printed soft robotic prosthetic hand with multi-articulating capabilities. *PLoS ONE*, 15(5). <https://doi.org/10.1371/journal.pone.0232766>
- Must, I., Kaasik, F., P.稗熹絕禎 僧 烷桦侵蝕 □J譜 廣簫麟U□P躍泌鉉 廉 Γ掣 玲公寮
康 舶貝 | I 鏡且 鉅 狂徒 疹 猗 糸 驛 汨 飢 m 躑 亢 鸞 忤 躡 切 耶 且 鐵 蝻 古 糸 決 奸 玖 旋 汴
蓬 代 乐 空 扼 歪 翦 蝟 九 蠹 □ 糗 樺 語 票 M 猓 象 公 □ 糗 樺 零 趨 佛 強 蠹 □ 糗

Rus, D., & Tolley, M. T. (2015). Design, fabrication and control of soft robots. *Nature*, 521(7553), 467–475. <https://doi.org/10.1038/nature14543>

List of Publications

El Atrache, A., Kim, D., Divo, E., & Drakunov, S. (2019). A dynamic model of helical dielectric elastomer actuator. *Electroactive Polymer Actuators and Devices (EAPAD) XXI*. Published. <https://doi.org/10.1117/12.2514382>

Park, J. H., Kim, D., Divo, E., & El Atrache, A. (2018). Optimization of helical dielectric elastomer actuator with additive manufacturing. *Electroactive Polymer Actuators and Devices (EAPAD) XX*. Published. <https://doi.org/10.1117/12.2296720>

Sikulskyi, S., Mekonnen, D. T., El Atrache, A., Divo, E., & Kim, D. (2021). Effects of Ferroelectric Fillers on Composite Dielectric Elastomer Actuator. *Actuators*, 10(7), 137. <https://doi.org/10.3390/act10070137>